

Research paper

Microstructural characteristics of the Whitby Mudstone Formation (UK)

M.E. Houben^{a,*}, A. Barnhoorn^b, J. Lie-A-Fat^b, T. Ravestein^b, C.J. Peach^a, M.R. Drury^a^a Faculty of Geosciences, Utrecht University, Utrecht, The Netherlands^b Faculty of Civil Engineering & Geosciences, Delft University of Technology, Delft, The Netherlands

ARTICLE INFO

Article history:

Received 10 June 2015

Received in revised form

7 November 2015

Accepted 15 November 2015

Available online 28 November 2015

Keywords:

Gas shale

Whitby mudstone

Posidonia shale

Ion-milling

Scanning electron microscopy

Gas adsorption

ABSTRACT

When trying to improve gas productivity from unconventional sources a first aim is to understand gas storage and gas flow potential through the rock by investigating the microstructure, mineralogy and matrix porosity of unfractured shale. The porosity and mineralogy of the Mulgrave Shale member of the Whitby Mudstone Formation (UK) were characterized using a combination of microscopy, X-ray diffraction and gas adsorption methods on samples collected from outcrops. The Whitby Mudstone is an analogue for the Dutch Posidonia Shale which is a possible unconventional source for gas. The Mulgrave shale member of the Whitby Mudstone Formation can microstructurally be subdivided into a fossil rich (>15%) upper half and a sub-mm mineralogically laminated lower half. All clasts are embedded within a fine-grained matrix (all grains < 2 μm) implying that any possible flow of gas will depend on the porosity and the pore network present within this matrix. The visible SEM porosity (pore diameter > 100 nm) is in the order of 0.5–2.5% and shows a non-connected pore network in 2D. Gas adsorption (N₂, Ar, He) porosity (pore diameters down to 2 nm) has been measured to be 0.3–7%. Overall more than 40% of the visible porosity is present within the matrix. Comparing the Whitby Mudstone Formation to other (producing) gas shales shows that the rock plots in the low porosity and high clay mineral content range, which could imply that Whitby Mudstone shales could be less favourable to mechanical fracturing than other gas shales. Estimated permeability indicates values in the micro-to nano-darcy range.

© 2015 Elsevier Ltd. All rights reserved.

1. Introduction

Gas in shales is trapped in poorly connected pores and sorbed on the surfaces of particles present in the matrix of the shale host rock. The bulk permeability of shales is so low that gas production from such formations is simply not feasible without fracturing the rock by injecting fluids at high pressure. This creates a radiating network of pathways that penetrate the shale formation around the injection and/or production well. Fractures induced in this way improve the overall permeability of the formation, both directly and by connecting pre-existing natural fractures. However, while much progress has been made in developing fracturing methods, the permeability of the gas shale matrix present between fractures is so low that very close fracture spacing is often needed to achieve sufficiently rapid transport of gas from the matrix into the induced fractures (Curtis, 2002; Gale et al., 2007). Improvements are

possible by increasing fracture density, but there is a limit and even the minimum achievable spacing may prove inadequate. Experience from the USA has taught us that petrophysical properties vary and a successful combination of petrophysical properties is hard to specify for gas shales, although almost all currently producing shale gas reservoirs are over mature, oil-prone source rocks; e.g.: Curtis, 2002; Jarvie et al., 2007.

In the Netherlands the lower Jurassic Toarcian Posidonia Shale Formation (PSF), the main hydrocarbon source rock in the North Sea, is considered as a possible gas shale (Herber and de Jager, 2010). The mean thickness of the formation in the subsurface of the Netherlands is 15–35 m, the average TOC value is 10% and the Hydrogen index (HI) is 800 (Herber and de Jager, 2010). The PSF is a generally dark grey, laminated and bituminous rock which represents peak transgression during a sea-level high stand and corresponds to an early Jurassic global oceanic anoxic event (e.g.: Trabucho-Alexandre et al., 2012). The PSF shales extend from the Yorkshire Basin (England; 'Whitby Mudstone Formation'), over the Lower Saxony Basin and the Southwest German Basin ('Posidonia Shale Formation') into the Paris Basin ('Schistes Carton') (e.g.:

* Corresponding author.

E-mail address: m.e.houben@uu.nl (M.E. Houben).

Jenkyns, 1985; Rullkötter et al., 1988; Littke et al., 1991).

In order to try and improve gas productivity from the shale matrix it is necessary to find ways to better connect the in-situ pore network to the natural and mechanical induced fractures. A first step is then to determine the pore network characteristics and the porosity values of the rock. Since in the Netherlands the PSF does not outcrop, for this research time equivalent exposed PSF samples have been collected north of Whitby (UK). For microstructural investigations, porosity and mineralogy measurements we used; a combination of a Precision-Ion-Polishing-System (PIPS) and Scanning Electron Microscopy (SEM), light microscopy, gas adsorption (N_2 , Ar, He), X-ray Diffraction, and X-ray Fluorescence.

2. Materials and methods

During the Jurassic the Cleveland Basin formed part of a system of shallow epeiric seas and small extensional tectonic basins linked to the North Sea Basin via the Sole Pit Basin (Ziegler, 1982; Powell, 2010). A Sinemurian–Aalenian paleogeographic map of the North Sea can be found in e.g.: Ziegler (1982), Littke et al. (1991), Knox et al. (1991), Hesselbo et al. (2000), Powell (2010). The organic-rich sediments deposited in Central and North Western Europe during the late Jurassic are known as the Mulgrave Shale (WMF), Schistes Carton (SC) and the Posidonia Shale (PSF) (e.g.: Jenkyns, 1985; Littke et al., 1991), where this depositional area was connected to the Tethyan ocean where black shales were deposited as well during the Jurassic (Littke et al., 1991). The Whitby Mudstones are similar to the fine-grained siliciclastic mudstone dominated successions deposited across North West Europe during the Lower Jurassic (Ghadeer and Macquaker, 2012) and consist predominantly of grey to dark grey mudstone and siltstone (Powell, 2010). Prior to exhumation the WMF has been carried to the early oil window (e.g.: Williams, 1986; Kemp et al., 2005), maximum burial depth of 2–4 km during the late Cretaceous (Hemmingway and Riddler, 1982; Williams, 1986; Green, 1989; Bray et al., 1992), and therefore these rocks could act as an useful analogue for shale reservoirs (Imber et al., 2014). Hydrogen indices in the Mulgrave Shale are high (Saalen et al., 1995), and some levels display unusually low $\delta^{13}C$ values (Jenkyns and Clayton, 1997; Kemp et al., 2005). The abundant framboidal pyrites in the section point towards anoxic and sulfidic conditions (Raiswell, 1982; Wignall and Newton, 1998). For an extensive summary on the geological history and geological setting of the Cleveland Basin and geological maps of the area around Whitby (UK) see e.g.: Powell (2010), Imber et al. (2014).

The WMF can be subdivided into the Alum Shale, the Mulgrave Shale and the Grey Shale. The Alum Shale Member, maximum thickness 37 m, consists of grey silty mudstones with bands of calcareous and siderite concretions (Powell, 2010). The Mulgrave Shale member is an oil-prone source rock, consisting of fissile, bituminous, dark grey mudstones with abundant ammonites (Powell, 2010), which is the lateral equivalent of the Posidonia Shale in Northern Europe (Leythaeuser et al., 1988; Rullkötter et al., 1988; Littke et al., 1991; Powell, 2010; Ghadeer and Macquaker, 2012). The Mulgrave Shale is a circa 30 m high section with TOC values ranging between 1 and 15% and the highest TOC values (4–15%) can be found in the bottom 8 m of the section (Hesselbo et al., 2000; Powell, 2010; Ghadeer and Macquaker, 2011; Imber et al., 2014). The bottom 8 m of the Mulgrave Shale is subdivided in sections due to thick bands of calcareous concretions of varying sizes (top to bottom: Curling stones, Whale stones, Cannon balls) and a limestone band near the top of the section (e.g.: Raiswell, 1976; Powell, 2010; Ghadeer and Macquaker, 2011; Imber et al., 2014). Below the Mulgrave Shale you can find a bioturbated paleo to dark-grey mudstone with concretionary siderite and calcite cemented units with TOC values below 4% called the Gray Shale

member (e.g.: Hesselbo et al., 2000; Powell, 2010). The transition from the Grey Shale to the Mulgrave Shale coincides with an increase of water depth in the basin (Saalen et al., 1996). Below the Whitby Mudstone one can find the Cleveland Iron Stone Formation. Ghadeer and Macquaker (2011) recognized six mudstone lithofacies types in the Cleveland Iron Stone Formation and the Whitby Mudstone Formation; 1. Sand- and clay bearing, silt-rich mudstones; 2. Silt bearing, clay-rich mudstones; 3. Clay-rich mudstones; 4. Clay-, calcareous nannoplankton-, organic carbon bearing mudstones; 5. Fine-grained muddy sandstones; and 6. Cement-rich mudstones, where lithofacies 3, 4 and 6 were encountered in the Mulgrave Shale member. Most siliciclastic clay-, silt- and sand-sized components are derived from detrital inputs to the basin (Ghadeer and Macquaker, 2011). In addition, some biogenic components are present like; bivalves, ammonoids, echinoderms, corals, calcispheres and foraminifers in addition to organic carbon (e.g. Saalen et al., 1996; Wignall et al., 2005). The difference in temporal grain size and composition is for this formation linked to the balance of primary biogenic production relative to the dilution and length of the sediment transport path, which varied during deposition (Ghadeer and Macquaker, 2011).

WMF samples investigated originate from outcrops along the cliff coast north of Whitby (UK) near the villages Runswick Bay and Port Mulgrave. Samples were collected during fieldwork (May 2013, March 2014) using a geological hammer and chisel. All samples studied were collected within 5 km laterally and samples were taken throughout the circa 8 m thick Mulgrave Shale member of the WMF, the organic-rich section. A method of plastic bags and cling film has been used to store and transport the samples; hence samples became air-dried during sample transportation/storage and before sample preparation. Hand specimens taken in the field were numbered chronologically based on when the sample was taken. These numbers are used here to distinguish between the different hand specimens. One hand specimen though could have been used to be studied with a number of different techniques (Fig. 1). One can distinguish between the different subsamples by the letter added to the initial number; T for thin sections investigated with light microscopy, P for PIPS-SEM samples investigated with Scanning Electron Microscopy, D for samples used for X-ray Diffraction, F for samples used for X-ray Fluorescence, H for He gas adsorption samples and B for N_2 and Ar gas adsorption samples. Different subsamples investigated with the same method are indicated with small letters (a–z) after the first capital letter indicating the method.

2.1. Optical microscopy

Polished thin sections were prepared (ca. 2.5×4 cm) using conventional methods for 5 samples collected throughout the Mulgrave Shale member, all spaced 1–2 m apart vertically. Samples used for thin sections originate from the same sample blocks as the PIPS-SEM samples (top to bottom of the section: 4, 6, 15, 1, 23) and can be directly linked to the PIPS-SEM samples based on characteristic beds present in the hand specimen (Fig. 2). These samples were investigated using plain- and cross-polarized light under a Leica microscope under transmitted light; digital images were taken with a pixel size of 0.1 μm .

2.2. PIPS-SEM

The sample blocks were subsampled into 2 mm thick slices taken perpendicular to the bedding with a maximum diameter of 8 mm. These subsamples were glued onto a modified 8 mm diameter SEM stub. After mechanical polishing of the top surface parallel to the stub the samples were mounted in a Gatan Precision

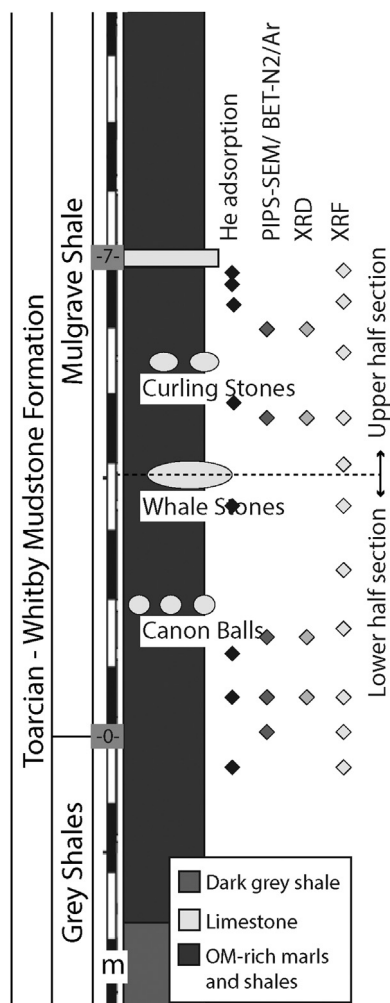


Fig. 1. Log modified after Hesselbo et al. (2000) with sample heights in the formation indicated for the samples used for He adsorption, PIPS-SEM/BET-N₂/Ar measurements, XRD and XRF. Furthermore the Mulgrave Shale section is subdivided in an upper and lower half by the black dotted line.

Ion Polishing System (PIPS; model 691) for a final polish of the top surface with Ar-ions. The PIPS used polishes the top surface with two Ar-ion beams at an angle of less than 10° to the surface, while during milling the sample was rotated to avoid striations on the polished surface. Samples were Ar-ion beam polished for 2 h using a 5.5 kV beam current and a maximal voltage of 50 μ A. After platinum coating the polished surfaces have been investigated using a Scanning Electron Microscope (SEM; FEI XL30S FEG-SEM, FEI Nova 600 Nanolab).

The first step in the SEM investigation was making a low resolution (pixel size = 1.8 μ m) Back Scattered Electron (BSE) overview image of the whole sample (circa 5,000 \times 5,000 pixels in total). Specific areas were then selected for high resolution BSE and Secondary Electron (SE) mosaics with a pixel size of circa 25 nm, to enable quantification of mineralogy and porosity. In order to make high resolution images of a large area, single SEM images were combined into one high resolution mosaic image (up to 100 images; e.g.: Desbois et al., 2009; Houben et al., 2013) using Microsoft ICE (Image Composite Editor). All SEM samples display a certain number of 50–100 μ m wide cracks, which are mostly artefacts of drilling, stress relaxation, storage and/or drying and are interpreted as not being part of the in-situ porosity of the samples. High

resolution mosaics were made in areas between the largest cracks. The magnification used for high resolution imaging (magnification 5000x, pixel lengths between 25 and 50 nm, mosaic size > 10,000 \times 10,000 pixels) was a compromise between a manageable number of images (ca. 100) and the micrograph resolution (Houben et al., 2014).

2.3. Image segmentation

By using a combination of thresholding and edge detection (Houben, 2013) the visible porosity in the SE images was segmented in MATLAB 2011 (The Math Works, 2011, Fig. 2). High resolution BSE, SE and segmented images were loaded into ArcMAP 10.1 (ESRI, 2012) so that the corresponding images overlap. The segmented SE image was afterwards transformed into a shapefile making it possible to correct the falsely segmented pores/minerals manually. The high resolution BSE images have been converted to mineral maps by means of their appearance and grey scales in ArcMAP 10.1 (ESRI, 2012). All minerals with diameter > 2 μ m visible in the matrix were manually traced where after they were classified based on their grey scales in the BSE images. The grey scales from black to white correspond to the following minerals: pores/cracks, organic matter, matrix/clay minerals/quartz/feldspar, calcite, dolomite, pyrite (Klaver et al., 2015a).

2.4. XRD measurements

Twenty grams of material from four selected samples has been sent to Q_{mineral} Analysis & Consulting for identification and quantification of the mineral composition of both the bulk and the clay fraction (clay minerals). Prior to the X-ray Diffraction (XRD) analysis the sample material was oven dried at 40 °C and ground for homogenization. 2.7 g of the sample were mixed together with 0.3 g of ZnO (used as a standard), and these were milled together in ethanol. After drying the sample was loaded into a XRD sample holder and analysed using CuK α radiation, see (Śrdoń et al., 2001) for detailed preparation method. For the quantification of the non-clay mineral fraction Rietveld analysis was performed (Rietveld, 1967) using the TOPAS software from Bruker (Bruker, 1999). The clay minerals were afterwards analysed separately by starting off with 5 g of the initial sample material. This initial sample material is selectively disintegrated from aggregates that incorporate clay minerals, like; carbonate cements, organic material, Fe-oxides and Fe-hydroxides (Jackson treatment; Jackson et al., 1976). Afterwards the < 2 μ m fraction of the samples was dissociated from the bulk sample by means of centrifugation. Next step was to exchange cations in the interlayer space of the sheetsilicates with CaCl₂ where after the Cl ions were removed by dialysis. What remained was used to prepare oriented clay samples that were used for the XRD analysis. The quantification of the clay minerals occurred using the PONKCS-method in the NEWMOD2 software (see: Moore and Reynolds, 1997; Scarlett and Madsen, 2006).

2.5. X-ray fluorescence

The analysed specimens were powdered using a mortar and disc mill, whereupon they were oven dried at a temperature of 70 °C for at least 24 h. The X-Ray Fluorescence (XRF) analysis was performed using a Panalytical Axios Max WD-XRF spectrometer and data evaluation was done using MINCOMP (Wolf, 2006; Regelink, 2014). This program was used to determine which minerals might be present in the rock sample with associated weight percentages (wt %), based on the elemental composition of the rock sample derived from the XRF analysis.

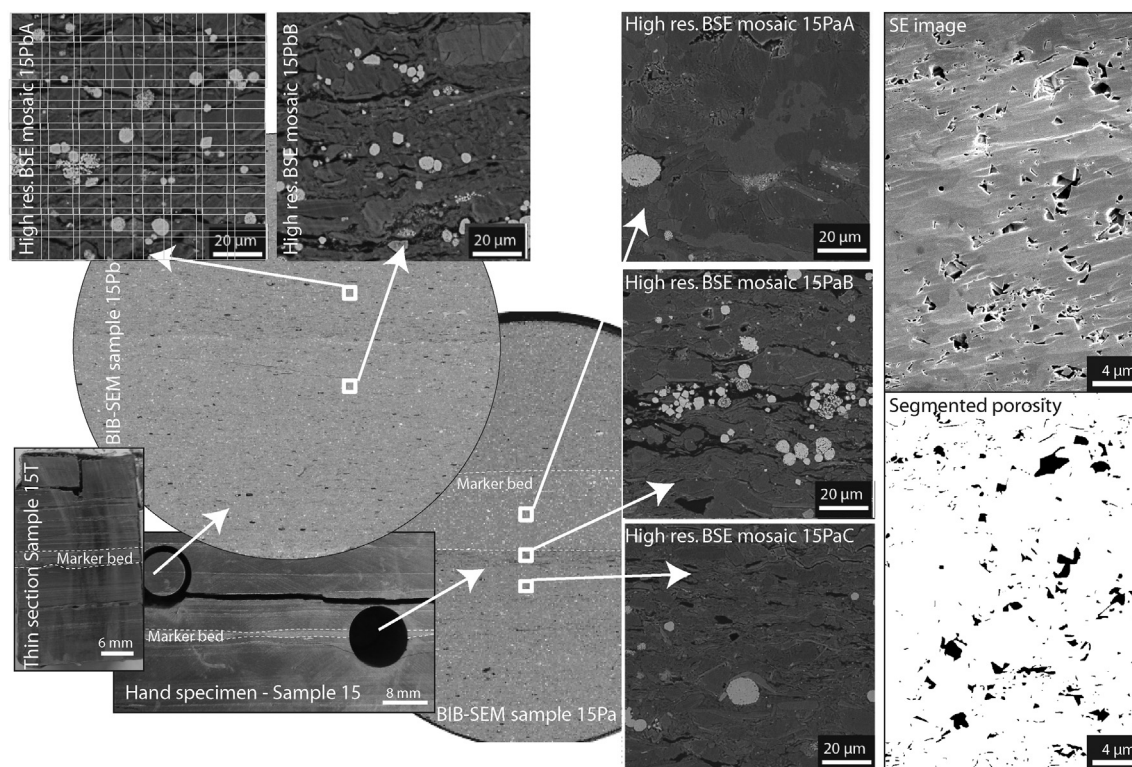


Fig. 2. Figure illustrates how the thin section and the PIPS-SEM samples can be directly linked to each other due to their location in the hand specimen of sample number 15. Furthermore, location of the high resolution mosaics is indicated in the PIPS-SEM samples and an example is shown for a SE image that is segmented into a pore map.

2.6. He pycnometry

Matrix density and porosity measurements were performed using the Ultrapycnometer 1000 version 2.12. The ultrapycometer measures volume and density of solid objects, in which helium has been used because of its small atomic dimensions. Both cylindrical (4 cm in length and 4 cm in diameter) and powdered samples (63–137 g) were subjected to matrix density measurements. The samples were powdered using a mortar and disc mill, whereupon they were oven dried at a temperature of 70 °C for at least 24 h. Cylindrical samples were used to estimate connected porosities (ϕ). The total volume of the sample (V_t) consists of both void space (V_v) and matrix (V_m). Since cylindrical samples were prepared, V_t can be calculated from the measured height and diameter and with V_m and V_t known the ϕ can be calculated. Because samples were manually polished, the total volume calculated assuming a perfect cylinder ($V_t = \pi r^2 h$) deviates slightly from the actual total volume of the sample. To increase accuracy an average for the height and diameter of a minimum of 12 measurements has been used. To estimate the deviation, a Phoenix nanotom μ CT scanner has been used to obtain real sample volumes. Results show that μ CT bulk volumes differ about 1% (averaging over 2 samples) from the calculated volumes, but one has to keep in mind that although rocks are visualized easily and non-destructively, beam hardening and the image processing can distort the μ CT image (e.g.: Nakashima et al., 2010; Ketcham and Hanna, 2014).

2.7. Gas adsorption measurements

Adsorption and desorption of Ar and N₂ gas on the surface of WMF subsamples has been done using a Micromeritics TriStar 3000. Subsamples were produced by breaking off small pieces (circa 200 mg) using a razor blade and a hammer. The piece was

then either used as a whole sample or crushed into a coarse powder. Prior to the gas adsorption measurements samples were either oven dried at 120 °C or vacuum dried (ca. 24 h both) to see whether the drying method used affected the measurements. A known amount of gas is then either admitted to or removed from the sample cell, allowing the Ar/N₂ gas to interact with the sample. As adsorption or desorption occurs, the pressure in the sample cell changed until equilibrium was reached. This enabled us to measure pressure differences between the amount of gas admitted/removed and the amount required to fill the void space. Standard procedure was used and hence analyses were performed at the boiling temperature of temperature of −195.8 °C (e.g.: Groen et al., 2003). Measuring the quantity of Ar/N₂ gas adsorbed over a range of relative pressures at a constant temperature results in the adsorption and desorption isotherms of the material, giving a measure of the internal void surface area of the samples using the Brunauer–Emmett–Teller (BET) method (Brunauer et al., 1938). The Harkins–Jura (Harkins and Jura, 1944) theory has been used to obtain a statistical thickness of the adsorbed gas layer ($2 < \text{pore diameter} < 100 \text{ nm}$). The thickness of the adsorbed gas layer is converted to a pore-size distribution by using the BJH technique assuming a cylindrical pore geometry (Barret et al., 1951).

3. Results

3.1. Microscopy

3.1.1. Mineralogy

Five thin sections were made of the WMF samples, the samples selected were numbered top to bottom of the Mulgrave Shale Formation: 4T, 6T, 15T, 1T, 23T. In general all samples show a shale microstructure with silt-sized fragments interbedded in a fine-grained matrix (grains < 2 μm in diameter). The two samples that

originate from the top 2 m of the Mulgrave Shale Formation (4T, 6T) display a homogeneous, matrix dominated microstructure, without any visible layers with different mineralogy on the mm–cm scale; bedding is visible due to preferred alignment of minerals and cracks. The three samples originating from the bottom 3 m of the Mulgrave Shale Formation (15T, 1T, 23T) show a mm-scale layered bedding of alternating grain dominated layers and matrix dominated layers. The matrix dominated layers in the upper half of the section consist of a mixture of large fossil fragments and some organic matter embedded in a fine-grained matrix, wherein also some single calcite, quartz, and feldspar grains ($>2\text{ }\mu\text{m}$ in diameter) were identified. Matrix dominated layers in the lower half of the section clearly show less fossil fragments (typically $<1\%$), but do show some quartz, feldspar, and calcite grains embedded within the fine-grained matrix. The grain dominated layers show a higher amount of isolated calcite/quartz grains ($>10\%$); furthermore the matrix in between the grains is more calcite rich. Besides, pyrite grains are evenly scattered throughout all samples.

Additionally subsamples (8 mm in diameter) of the WMF blocks (4P, 6P, 15Pa, b, 1P, 23P) were PIPS polished and SEM imaged. The PIPS-SEM samples could be directly linked to the thin sections based on their location in the sample blocks (Fig. 2). High resolution mosaics were made within different layers of the PIPS-SEM samples and by using the box count method (Kameda et al., 2006) the Representative Elementary Area (REA) has been determined following the methodology as described in Houben et al. (2013) under the assumption that porosity in the clay is linked to the mineralogy and mineral distribution. A sample can be homogeneous on the 8 mm diameter scale, but could also show layering with some layers being more carbonate, organic matter or quartz rich. The here identified REA is the minimum area within one mineralogical distinct layer in a PIPS-SEM sample that has to be imaged to get the representative mineralogy for that particular layer. A starting box size of 100×100 pixels has been used and this was systematically increased with 100 pixels in both x and y directions (Houben et al., 2013) taking; organic matter, matrix, pyrite, and minerals (grains with diameter $>2\text{ }\mu\text{m}$) into account. The REA has been reached when the box size becomes larger than $150 \times 150\text{ }\mu\text{m}$.

High resolution mosaics of samples from the upper half of the section (4P, 6P; Fig. 3) show up to 25% of highly porous, irregular shaped, large (up to $40\text{ }\mu\text{m}$ long) fossils that together with the matrix account for most of the porosity in these samples. Furthermore, the organic matter content is 6–9%. In addition, the microstructures encountered (4P, 6P) are comparable, and no layering due to alternating mineralogy is visible in the PIPS-SEM samples. High resolution mosaics of PIPS-SEM samples 15PaA; 15PaB, B; 1PA, C; and 23PA, B, C, (Fig. 3) all show similar microstructures of minerals (quartz, dolomite, calcite, (framboidal) pyrite) up to circa $10\text{ }\mu\text{m}$ in diameter embedded in a fine grained matrix and an organic matter content ranging from 5 to 11%. Mosaic 1PB (Fig. 3) shows a greater fraction of larger (circa $10\text{ }\mu\text{m}$ in diameter) minerals than the previous group of mosaics. In addition the organic matter content in this mosaic is circa 1%. Mosaic 15PaB (Fig. 3) has been made within a Calcite-rich layer, where the calcite in this layer is mostly present as cement and/or grains which both lack visible porosity. The relative high porosity present in this mosaic is due to a few (less than 10) up to $10\text{ }\mu\text{m}$ wide pores. In addition this particular layer (15PaB) features almost no organic matter ($<0.5\%$). Mosaic 15PaC displays the highest organic matter content which is interlayered with the matrix and features some porosity. Overall the amount of pyrite found in all the PIPS-SEM mosaics varies from 2 to 6%. Organic matter content varies between less than 0.5% up to 17%, where the two layers with the extreme values are found in sequence in sample 15Pa.

3.1.2. Porosity, pore morphology, pore size distribution

Visible SEM porosity is in the range of 0.6–3.0% in all imaged high resolution mosaics ($25\text{ nm} < \text{pixel length} < 50\text{ nm}$). The majority of the segmented pores ($>600,000$) occur in the matrix which overall shows a 0.5–4.5% porosity in the different mosaics. Pore morphologies found in the WMF samples are similar to pores present in other shales and can be classified according to Desbois et al. (2009), Heath et al. (2011) and Loucks et al. (2012). Intergranular pores (Types I–III; Desbois et al., 2009) are present in the matrix where highest matrix porosity coincides with a low overall matrix content in the mosaic. Furthermore, microcracks (Type V; Heath et al., 2011) mainly present in the matrix or along minerals were identified in all PIPS-SEM samples as well as in the thin sections. Microcracks have high aspect ratios, sharp crack tips and rough edges and make up 4–17% of the total porosity visible in the mosaics. Although most of the organic matter present does not show any porosity (Klaver et al., 2015a), both samples 15P (a, b) do show organic matter pores (Fig. 4a–f). These are either round pores with smooth pore walls, irregular shaped pores, or pores present in a mineral organic matter mixture (see also Klaver et al., 2015a). Loosely packed single non-porous pyrite grains that are forming framboidal pyrite show intergranular porosity (Type VII; Heath et al., 2011), accounting for 0.5–3.5% of the total porosity present (Fig. 4g, h). In addition, sheet silicates encountered show very elongated smooth walled pores in between the single sheets (Fig. 4i,j; e.g.: Houben et al., 2013; Klaver et al., 2015a; Loucks et al., 2012). Furthermore, highly porous and irregular shaped large (up to $40\text{ }\mu\text{m}$ long) calcareous fossils account for 40–45% of the total porosity when present in the mosaics (mainly 4 and 6), pores show angular edges with smooth pore walls (Fig. 3k,l) and are unconnected in 2D.

Most mosaics show segmented pores in the matrix which have equivalent diameters below $11\text{ }\mu\text{m}$, where the exception is mosaic 15PaB showing pores (4) with equivalent diameters up to $18\text{ }\mu\text{m}$, forming the upper bound of the pore network limited by the area imaged (Fig. 5a). Most imaged pores have equivalent diameters in the range of $72\text{--}300\text{ }\mu\text{m}$ (Fig. 5a). Due to image resolution pores become less visible at the low end when they have equivalent diameters below 144 nm resulting in a practical pore resolution (PPR; Klaver et al., 2012) of about 30 pixels. The size distribution of the resolved pores in the SEM mosaics (pores $> \text{PPR}$) fit a power law area distribution (Houben et al., 2013), with a power law exponent (D) between 1.97 and 2.31 (Fig. 5b). The lowest values for D can be linked to the mosaics with a low matrix ($<60\%$) and organic matter ($<2\%$) content (15aB, 1B). These mosaics also have less total visible pores segmented, which is not reflected in the total porosity value of the mosaics due to the fact that pores encountered are larger on average. The area size distribution of pores in the clay follow a power law distribution for all mosaics, where the minimum pore area size varies due to a slight variation in pixel length ($25\text{--}50\text{ nm}$). Overall pores in the matrix with areas $10^4\text{--}10^8\text{ nm}^2$ follow a power law size distribution with a power law exponent of 2.1 ± 0.06 and a constant of proportionality ($\log C^*$) of -1.86 ± 0.354 , where the 95% confidence level has been used as an uncertainty for the best fit (Klaver et al., 2012, Fig. 5b). To see whether or not this pore size distribution holds for smaller pore areas one mosaic (red crosses in Fig. 5b (in web version)) was made with a pixel size of 6 nm (imaging pores in the matrix mainly). The equivalent pore diameter where we found a cut-off due to resolution was at 102 nm , where pores with diameter $102\text{--}144\text{ nm}$ do follow a similar size distribution trend as pores with equivalent diameter $>144\text{ nm}$.

3.2. X-ray diffraction

The mineralogy of four samples (4D, 6D, 15D, and 1D; Fig. 1) has been investigated using X-ray diffraction (XRD). Results of the XRD

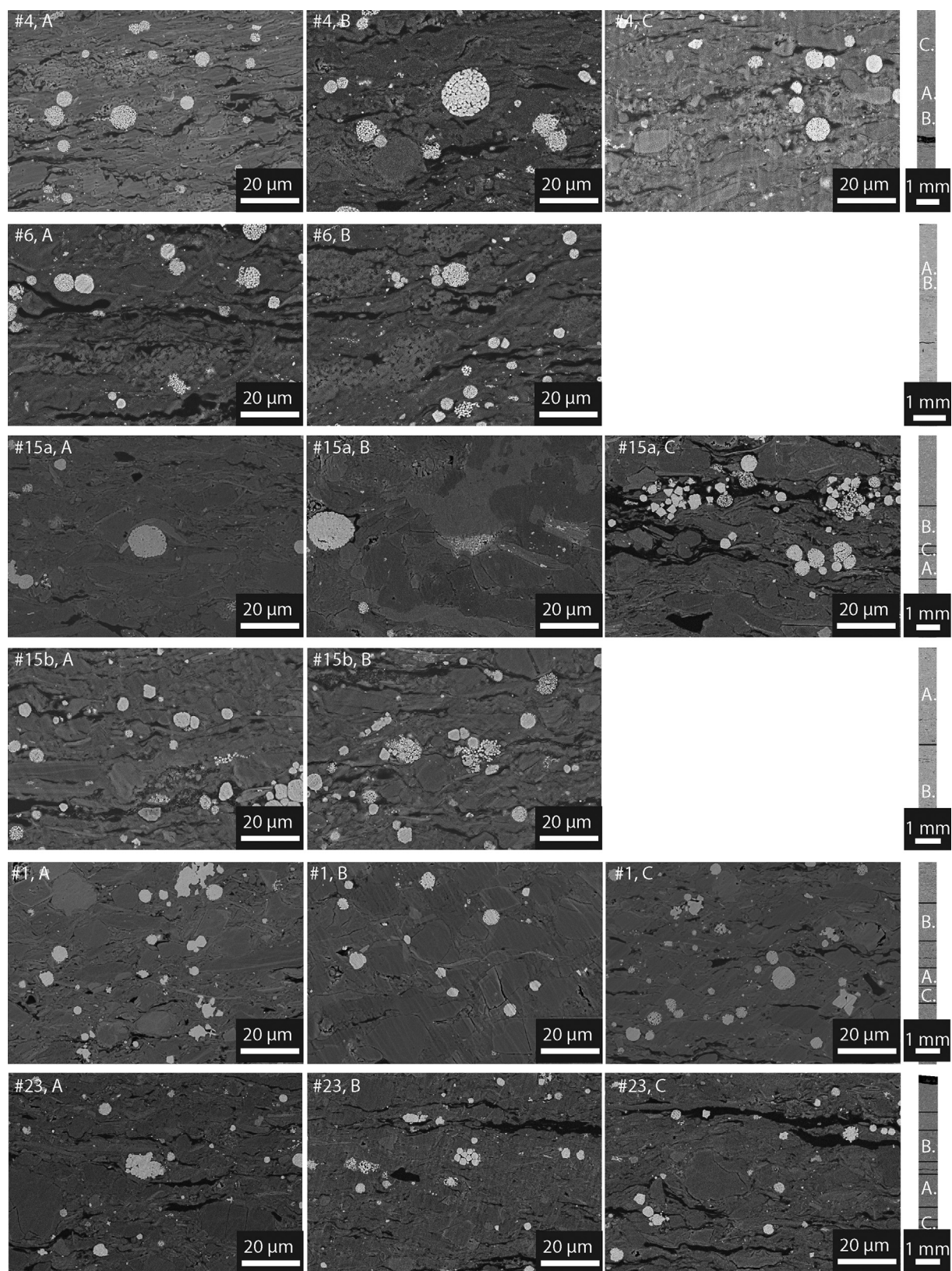


Fig. 3. Overview of the different high resolution SEM mosaics made at different locations within the PIPS-SEM samples, where PIPS-SEM sample overviews can be found to the right of the high resolution mosaics with an indication of the layer the high resolution mosaics were taken in. All high resolution mosaics show framboidal pyrite (white), and more or less organic matter (black). Furthermore, different shades of gray represent different minerals (quartz, carbonates, feldspar, clay minerals) and the clay matrix (grains with diameter < 2 µm).

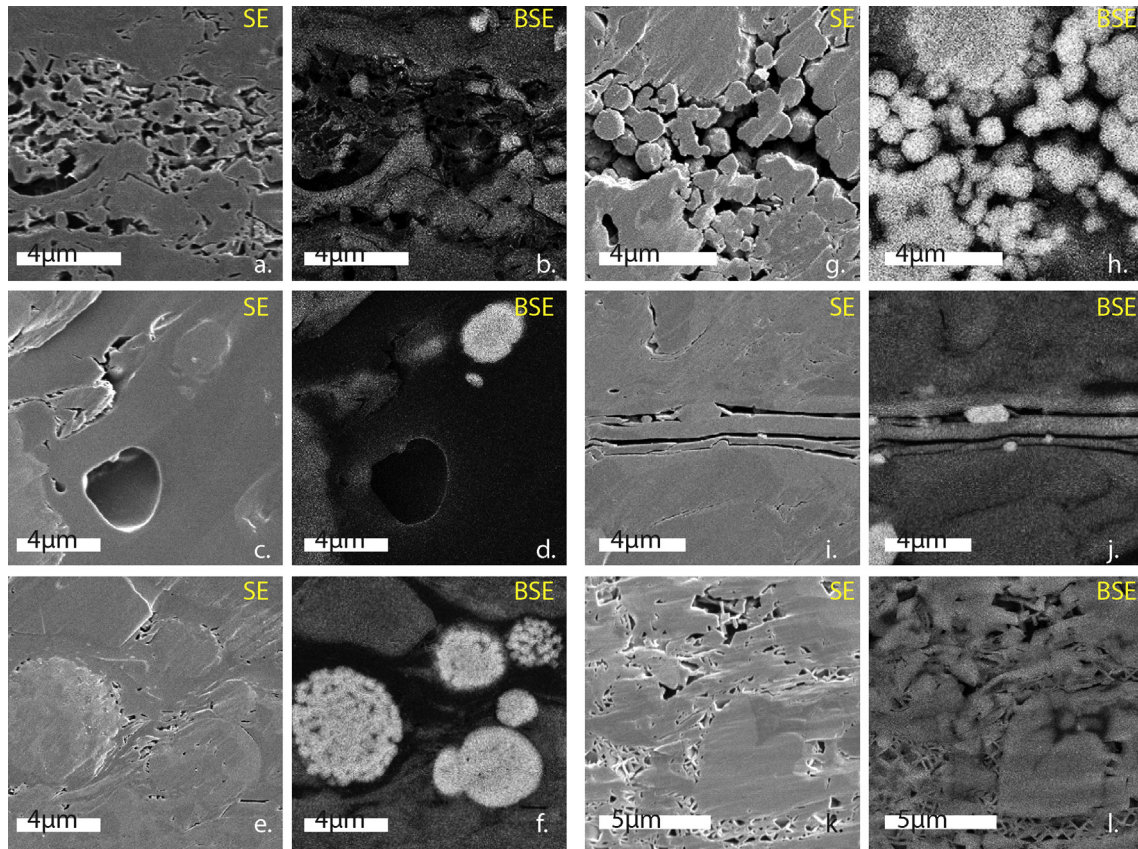


Fig. 4. Pore structures in 2D encountered in different minerals and mineral aggregates. a–f. Side by side one can find the corresponding BSE and SE images of pores in organic matter. g–h. SE and BSE image of pores in a framboidal pyrite, pores in between single pyrite grains. i–j. Pores in sheet silicate. k–l. Pores in a carbonate fossil.

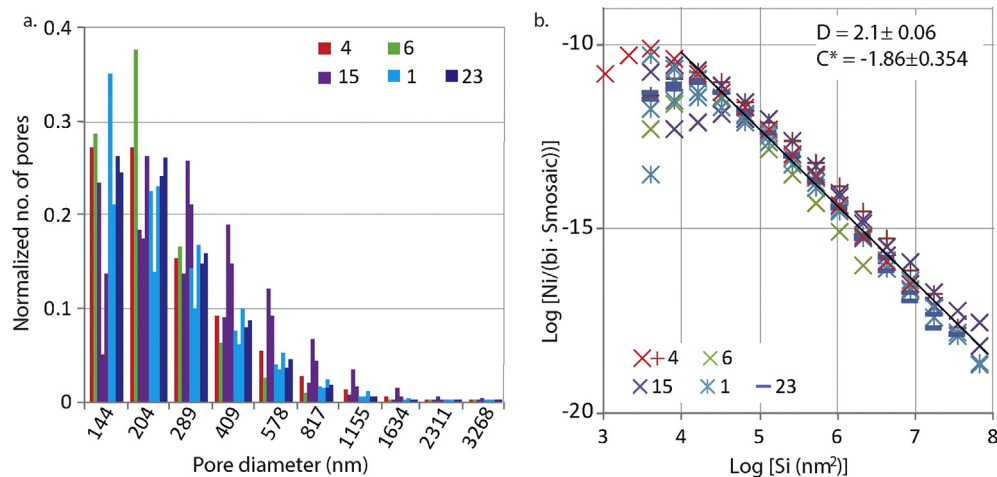


Fig. 5. Pore size distributions encountered in the different SEM mosaics. a. Number of pores versus pore diameter shows the general size distribution for pores in the clay matrix as encountered. Pores with diameters below 144 nm are not distinguished from the background due to the pixel size used for imaging. b. Normalized pore size distribution of the pores in the clay matrix, the log of the normalized number of pores (no. of pores with and area smaller than size i divided by the size of the mosaic and the bin size) versus the log of the pore area shows that generally the size distribution in all mosaics is comparable.

bulk measurements and the clay fraction in detail can be found in Table 1. The main fraction of the mineralogy exists of sheet silicates, where this value is slightly higher for the samples from the lower half than for the upper half (68.4–69.9% and 51.3–59.4% resp.), where the 2:1 Al/Fe sheetsilicates content seems to be homogeneous throughout the section, but the kaolinite content is higher in the lower half than in the upper half. The silicate content is constant

throughout the section varying from 13.1 to 17.6%, just as the oxide (0.7–1.1%), sulphide (7.7–11%) and sulphate (0–0.9%) contents. Largest variation can be found in the carbonate content varying between 12.1 and 26.1% in the upper half of the section (4D, 6D) and 3–4.5% (15D, 1D) in the lower half of the section. The XRD clay mineral fraction results add information about the specific clay minerals encountered. No real trends between lower half and

Table 1
Results of the XRD measurements for four samples, top to bottom of the section: WMF4, WMF6, WMF15, WMF1.

Sample no.	Formation height	Bulk measurements															Clay fraction																			
		2:1 Al/Fe sheetsilicates															Gypsum					Illite/Smectite					Kaolinite					Chlorite				
		Kaolinite	Chlorite	Quartz	Plagioclase	Chabazite	Calcite	Ankerite	Goethite	Anatase	Rutile	Pyrite	Markasite	Gypsum	Illite/Smectite	Illite	Kaolinite	Chlorite																		
4D	6.0	38.1	11.5	1.7	13.1	0.0	0.0	25.1	1.0	0.1	0.6	0.1	7.7	0.0	0.9	54.0	17.0	26.0	3.0																	
6D	4.5	40.4	15.1	3.9	15.2	0.7	0.1	12.0	0.1	0.0	0.6	0.1	11.0	0.0	0.7	31.0	27.0	39.0	4.0																	
15D	1.8	42.1	23.5	2.8	16.3	1.0	0.3	1.7	2.8	0.0	0.9	0.1	8.0	0.4	0.0	42.0	17.0	38.0	3.0																	
1D	0.5	43.9	22.6	3.4	16.0	0.9	0.4	1.3	1.7	0.1	0.7	0.3	8.5	0.2	0.0	38.0	19.0	40.0	3.0																	

upper half of the section can be found. Interlayered illite/smectite content varies between 31 and 54%, kaolinite content between 26 and 40%, illite content from 17 to 27% and the chlorite content is between 3 and 4% for all samples. The two samples from the lower half are comparable, whereas the two samples from the upper half show differences in illite/smectite, illite and kaolinite contents (Table 1).

3.3. X-ray fluorescence

Based on the elemental analysis, the mineral composition of the different samples was determined with associated element weight percentages (wt %) by using MINCOMP (Wolf, 2006; Regelink, 2014). On average the XRF results contain an uncertainty of $\pm 4.5\%$, and the values were normalized to 100%. Eleven samples were analysed throughout the Mulgrave Shale member (Fig. 1). The results show that the quartz content is more or less constant in the Mulgrave Shale member (14–17.8%). Clay contents measured show that all values are higher than 45%, with a maximum of 70%. Calcite content increases towards the Whale Stones and decreases towards the bottom of the section. Furthermore, clay and calcite contents show a negative correlation. In addition, pyrite content is relatively homogeneous, but close to the Whale Stones the pyrite content increases. Other minerals encountered in the WMF are goethite and chlorite with average contents of 5–6%. WMF is very clay-rich, though the clay content seems to decrease towards the Whale Stones (Table 2).

3.4. He pycnometry

Porosity measurements with He pycnometry were performed on 8 samples (Fig. 1) and porosity values measured vary between 0.3 and $6.9\% \pm 1.01\%$ due to the fact that the measured samples were not perfect cylinders. These porosity values represent values of porosity connected to the samples outside that He can reach, hence porosity not connected to the samples outside cannot be reached and is not incorporated in this value. Matrix densities measured on cylindrical samples vary between 2.25 and 2.55 g/mm³ and matrix densities measured on powdered samples vary between 2.21 and 2.80 g/mm³ (Table 3). Generally the matrix densities measured on powder samples are slightly higher than the ones measured on cores, due to the fact that the He has better access to the pore space in the powdered samples. The low density of organic matter influences the overall matrix density of the rock, hence low density values of a sample can point towards higher TOC values (e.g.: Passey et al., 2010) or represents a lot of unconnected porosity that is present in the sample. The results show no correlation between height in the section, porosity and whether the samples were taken parallel (transverse), perpendicular (longitudinal) or at a 45° angle (diagonal) to the bedding (crack formation is preferred parallel to the bedding). Results show that samples taken from the same block and therefore from the same height show a variation in porosity, suggesting a cm scale variation in porosity laterally (Table 3). All matrix densities measured on cylinders taken from the upper half of the section (above the Whale Stones) were similar whereas the densities measured on samples from the lower half show an increase towards the bottom (Table 3). Furthermore, no correlation has been found between porosity and matrix density or organic matter content (measured in the PIPS-SEM samples) and matrix density.

3.5. Gas adsorption (BET)

All samples investigated were grouped into two end-member phases, namely; dark grey clay subsamples and laminated

Table 2

Mineralogy of the XRF results summarized for the WMF samples.

Sample no.	Formation height	Illite	Smectite	Kaolinite	Quartz	Calcite	Pyrite	Goethite	Chlorite	Other
47F	6.8	23.1	10.26	30.7	15.2	3.69	4.16	5.33	6.1	1.43
97F	6.5	25.53	5.97	19.86	14.1	14.72	9	4.24	5.42	1.17
59F	5.5	25.4	5.32	25.36	17.1	9.66	4.78	4.62	6.53	1.26
5F	4.5	20.62	6.36	23.67	14.1	17.84	5.18	6.07	4.84	1.29
95F	4.0	25.74	11.4	9.42	14	13.68	11.45	3.82	5.71	4.81
70F	3.5	25.24	10.49	15.07	15.6	11.58	9.6	3.45	6.31	2.65
80F	2.5	28.72	9.31	16.8	15.8	6.49	9.2	3.39	6.2	4.04
29F	1.7	24.12	5.99	31.17	17.7	2.7	4.77	5.03	7.08	1.48
3F	0.5	25.67	10.75	29.92	15.1	1.63	3.91	5.4	6.22	1.44
22F	0.0	25.49	10.83	30.14	15.1	3.8	3.04	4.26	5.97	1.43
45F	−0.5	25.84	9.94	28.1	17.8	1.16	4.58	5.01	6.19	1.4

Table 3

He pycnometry results showing formation height of the samples, matrix density and porosities measured.

Sample	FM. Height (m)	Matrix density (g/mm ³)	ϕ (%)
47Ha	6.8	2.44	2.62
47Hb	6.8	2.45	2.02
47Hc	6.8	2.54	2.57
49Ha	6.6	2.51	5.14
49Hb	6.6	2.47	3.91
49Hc	6.6	2.5	4.58
49Hd	6.6	2.42	3.02
49He	6.6	2.46	5.15
49Hf	6.6	2.53	4.3
49Hg	6.6	2.53	6.88
53H	6.3	2.48	4.14
56Ha	4.9	2.44	0.77
56Hb	4.9	2.41	5.82
70Ha	3.5	2.26	2.58
70Hb	3.5	2.25	4.76
70Hc	3.5	2.26	2.51
70Hd	3.5	2.25	4.55
29Ha	1.25	2.42	1.1
29Hb	1.25	2.42	0.26
2Ha	0.5	2.55	1.09
2Hb	0.5	2.51	3.76
2Hc	0.5	2.52	4.95
45Ha	−0.5	2.44	3.6
45Hb	−0.5	2.44	4.54
45Hc	−0.5	2.41	1.94
45Hd	−0.5	2.47	5.33

(calcite/quartz-clay) samples. BET surfaces measured with N₂ are in the range of 0.66–11.98 m²/g and the corresponding porosity values ranged from 0.4 to 4.7%. Measured Ar gas BET surfaces are 2.36–7.04 m²/g and the corresponding porosity values ranged from 0.83 to 5.56% (Table 4). The clay rich vacuum dried samples showed a porosity of 0.4–1.5%, whereas the clay-rich oven dried samples have measured porosities in the range of 2.4–3.3%. When using Ar to measure the porosity, values ranged from 0.8 to 5.6% for the clay rich samples. N₂ BET porosity in the laminated samples showed values ranging from 3.6 to 4.7% for the oven dried samples and 2.6–3.0% for the vacuum dried samples. Ar porosities measured are in the range of 3.01–3.04%. BET measurements show that vacuum drying in general results in a lower porosity value than oven drying (at 120 °C). It could be that these particular selected samples were less porous and that pores with diameters between 5 and 20 nm were not present, but more likely is that samples were less dried when the vacuum pump was used instead of oven drying implying that an amount of pores was still blocked with water/gasses and that prevented the N₂ gas from entering the sample, resulting in an overall lower porosity value (Olphen van, 1977; Yang and Aplin, 1998; Keller et al., 2011). Overall the layered samples show a slightly higher BET porosity than the clay samples (Fig. 6a).

Furthermore, clay rich samples originating from the lower half of the Mulgrave Shale (15B, 1B, 23B) do show a slightly higher BET porosity than the samples from the upper half of the section (4B, 6B), where one has to keep in mind that these porosity values tell us something about the connected porosity that can be reached by Ar/N₂ from the samples outside. The pore size distribution graph shows a < 0.5% porosity contribution for pores with diameters between 10 and 100 nm, contributing to the porosity most are pores <10 nm in diameter (Fig. 6b).

4. Discussion

4.1. Mulgrave Shale

4.1.1. Mineralogy and microstructure

The Mulgrave member of the Whitby Mudstone Formation is a mudstone with generally between 50 and 70% of sheet silicates (XRD and XRF measurements) and on average > 50% matrix in the BIB-SEM mosaics (Fig. 7a). Other minerals encountered in the XRD, XRF and SEM measurements are; silicates (mainly quartz), carbonates (mainly calcite), sulphides (mainly pyrite), oxides (goethite, anatase, rutile) and sulphates (gypsum). The SEM mosaics do show detail on the mm-scale layering mainly present in the lower half of the section that is neglected with both XRD and XRF measurements due to the fact that bulk measurements were done on powdered samples of cm size. That the anisotropy in the Mulgrave Shales is high (up to 30%) due to the high clay content was also shown by acoustic velocity measurements (Zhubyayev et al., 2016). Although the XRD/XRF sheet silicate values and the SEM matrix values seem to correspond for the different samples, the silicate and sulphide contents were underestimated using the SEM mosaics to quantify the mineralogy. Pyrite contents measured in the SEM mosaics vary between 3 and 5%, whereas the XRD/XRF values show pyrite contents of 4–11%. This discrepancy could be due to the fact that there is a certain percentage of pyrite minerals present below the resolution used for imaging, but could also be due to the fact that SEM mineralogy is measured in a 2D section though XRD/XRF is measured on a 3D powder in 2D smaller crystals are less likely intersected and an intersection plane rarely cuts the mineral where the diameter is largest, for spheres though the mean intersection length is close to the true 3D size of the object (Higgins, 2000). In addition the underestimation of the silicate content in the SEM mosaics could be related to the size of the quartz grains (below resolution used for imaging), but is also related to the colour of these minerals in the BSE mosaics, generally the silicates have a similar colour as the sheet silicates making it hard to distinguish the silicates from the background (matrix). This is especially true for samples originating from the upper half of the section (4, 6). The XRD/XRF measurements show a silicate content of 13–17%, whereas in the SEM images only ca. 3% of silicates has been

Table 4

Results of the Ar and N₂ gas adsorption measurements, where the samples are ordered top to bottom of the Mulgrave Shale section. Both clay matrix rich and samples that display mm-scale layering were investigated (see description). Furthermore, the different drying methods; oven drying at 120 °C (120) and vacuum drying (Vac) are indicated in the Drying method column. .

Gas	Sample	Formation height	Description	Shape	Drying method	Porosity	BET surface area (m ² /g)
N ₂	4Ba	6.0	Clay	Block	120	2.39	4.78
N ₂	4Bb	6.0	Clay	Powder	Vac	1.49	2.31
N ₂	4Bc	6.0	Clay	Block	Vac	0.42	0.66
N ₂	4Bd	6.0	Clay	Thin slice	Vac	1.34	2.61
N ₂	4Be	6.0	Clay	Powder	120	2.97	5.06
Ar	4Bf	6.0	Clay	Block	120	1.50	3.71
Ar	4Bg	6.0	Clay	Powder	120	2.69	3.71
Ar	6Ba	4.5	Clay	Block	120	0.83	2.36
N ₂	15Ba	1.7	Layered	Block	120	3.64	7.72
N ₂	15Bb	1.7	Layered	Block	120	4.62	10.24
N ₂	15Bc	1.7	Layered	Powder	Vac	2.57	7.48
N ₂	15Bd	1.7	Layered	Block	Vac	2.63	7.53
N ₂	15Be	1.7	Layered	Thin slice	Vac	3.02	8.68
N ₂	15Bf	1.7	Layered	Powder	120	4.74	11.98
Ar	15Bg	1.7	Layered	Block	120	3.04	7.04
Ar	15Bh	1.7	Clay	Block	120	1.93	4.98
Ar	15Bi	1.7	Layered	Powder	120	3.01	7.04
Ar	15Bj	1.7	Clay	Powder	120	5.56	4.98
N ₂	1Ba	0.5	Layered	Block	120	3.94	8.92
N ₂	1Bb	0.5	Clay	Block	120	2.82	6.61
Ar	1Bc	0.5	Clay	Block	120	1.57	5.50
N ₂	23Ba	0.0	Clay	Block	120	3.32	7.58
Ar	23Bb	0.0	Clay	Block	120	1.78	4.97

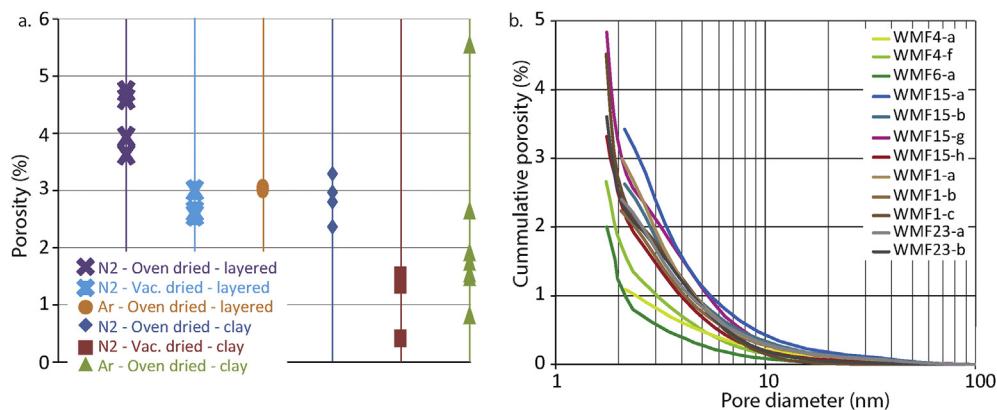


Fig. 6. a. BET results sorted by drying method and sample kind. b. All BET results sorted by sample where the Ar results are shown in red and the N₂ results are shown in blue.

observed in samples 4 and 6. Due to the fact that the silicate minerals are larger in the SEM mosaics of samples taken from the lower half of the section (15, 1, 23) the SEM silicate content here (9–14%) reflects the silicate content in the XRD/XRF measurements better (14–18%), although it is still slightly underestimated. The carbonate content highly varies throughout the section (2–26%) and mainly depends on the relative sample position in the WMF. The carbonate contents based on the SEM mosaics are similar to XRD/XRF values. Minor amounts of gypsum (XRD), goethite (XRD, XRF), anatase (XRD), and rutile (XRD) were distinguished using XRD/XRF. Organic matter content was on average 7–8% in the PIPS-SEM samples.

4.1.2. Porosity WMF

Porosity values in general strongly depend on the measuring method used and is furthermore influenced by the burial history and diagenesis of the rock through geological time. According to Yang and Aplin (1998) the porosity of mudstones from the Norwegian margin with 50–55% clay decreased from 27 to 12% when the effective stress changed from 16 to 28 MPa. For the Whitby

Mudstone porosity values found are 0.3–6.9% for He adsorption, 0.4–5.6% for Ar/N₂ adsorption and 0.6–3.0% for the SEM measurements, implying more compaction of the starting material of the WMF than the Norwegian margin samples (Yang and Aplin, 1998) possibly due to the higher amount of clay minerals present in the WMF samples or the higher effective pressure the rock have been exposed to (deeper burial) or a combination of both. Porosity varies for the different methods used because of the fact that different kinds of porosity were measured, connected porosity to the samples outside that can be reached by a certain gas for the He, Ar and N₂ adsorption and visible porosity in the SEM images (depending on the image resolution). Furthermore, porosity also varies between different WMF samples and is not only depending on sample height in the Mulgrave Shale section but also varies when the porosity has been measured for different subsamples originating from one sample block (Fig. 7b) implying a lateral variation on the cm scale as well as variations across the bottom 8 m of the Mulgrave Shale section. The Ar/N₂ BET data does not show a significant difference in porosity with respect to the two used gasses, which is in agreement with the molecular radii of the

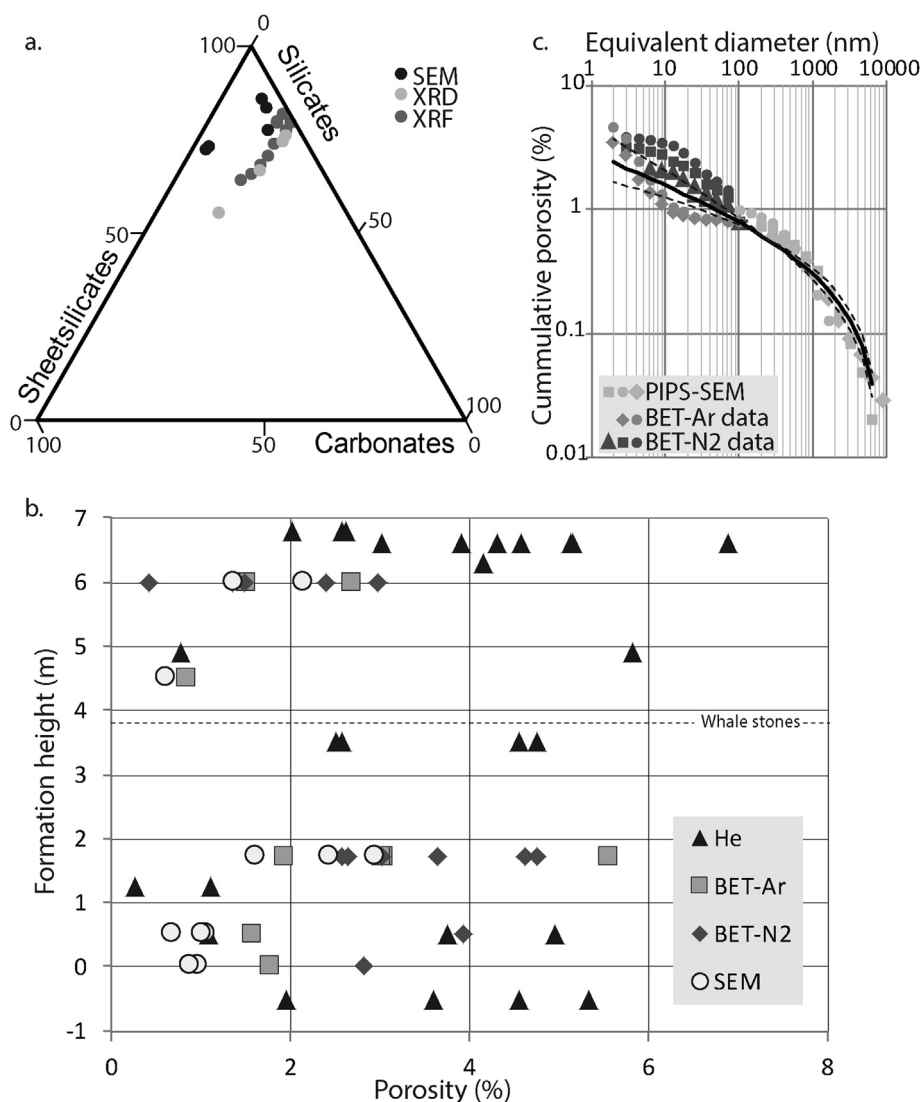


Fig. 7. a. Mineralogy of the WMF as measured using SEM mosaics (black), XRD (light grey) and XRF (dark grey). b. Comparing porosities measured using different measuring methods on samples originating from different heights in the Mulgrave Shale Section of the WMF. In general $\phi_{SEM} < \phi_{BET} < \phi_{He}$, and porosity varies for different samples from the same height, there is no ϕ trend observed throughout this section. c. This graph shows the cumulative porosity versus the pore diameter of both the SEM and the BET data obtained for sample 4. Pore size distribution of the pores in the SEM images of sample 4 extrapolated to smaller pore sizes when the pores are assumed to follow the same size distribution results than in the black line. Comparing the extrapolated porosity to the adsorption data shows that the model follows the N_2 data best and that the adsorption results are best represented by the high end values of the model.

two gasses (Ar: 106 pm, N: 71 pm). The results do show that different drying methods influence the outcome (ϕ vacuum drying $< \phi$ oven drying; Table 4) and furthermore that sample state (ϕ powder $> \phi$ block; Table 4) also has an influence due to the fact that you increase the surface area adsorption when measuring powder samples. In general we can say the $\phi_{SEM} < \phi_{BET}$ (Ar, N_2) $< \phi_{He}$, but the 2D porosity values of the SEM measurements can only be compared to 3D pore size distributions (He, Ar, N_2 data) when it is assumed that the mosaic areas investigated are large enough to represent all different pore shapes in 2D found in a certain layer (e.g.: Houben et al., 2014; Klaver et al., 2012). Furthermore, for the BET measurements relative pressure is related to a pore diameter, which can be turned into pore areas only when we assume that these pores are tubular shaped and that the circular cross-section of the tube is the corresponding pore area. In addition, what has to be noted is that gas adsorption–desorption measurements measure pores with diameters between ca. 2 and 100 nm, whereas the high resolution mosaics were made at such a

magnification that the smallest pores visible in representative amounts have equivalent pore diameters >140 nm. Combining the PIPS-SEM and BET results then gives an estimate of the minimum total porosity value down to a pore diameter of 2 nm, assuming that PIPS-SEM and BET porosities do not show any overlap and can be added up. The minimum total calculated porosity is between 3.9 and 5.3% for sample 4 and between 4.4 and 7.8% for sample 15 and these values are comparable to the He porosities of similar samples (Fig. 7b).

4.1.3. Pore size distributions WMF

Both results from the N_2 /Ar adsorption and the SEM images can be turned into pore size distributions (Figs. 5a and 6 b) for the methods used resolution. It is obvious that smaller pores occur more frequently than larger pores until the resolution of the method has been reached (e.g.: Fig. 5a). The fact that pores with diameters between 2 and 100 nm were measured with the adsorption method furthermore shows that there are open spaces

(grain boundaries, pores) present below the resolution used for SEM imaging, which is confirmed by the He porosities showing higher values than the SEM or N₂/Ar adsorption data. The power law exponent values (D), calculated for pores in the SEM mosaics with cross-sectional areas between 32,767 and 33,554,431 nm², show that pores in the matrix in mosaics with more than 60% of matrix display a higher D -value. This indicates that smaller pores contribute to the porosity more for areas with more clay. That clay content influences the porosity and pore throat sizes was also seen by Yang and Aplin (1998) for clays from the Norwegian margin they found that the siltier the sample the higher the porosity and the less well sorted the pore throat size distributions. Pores in the WMF matrix follow an exponential size distribution with an average power law exponent of 2.1 ± 0.06 and a constant of proportionality ($\log C^*$) of -1.9 ± 0.35 . Assuming that smaller pores not visible in the SEM mosaics are following the same size distribution as the visible SEM pores gives an idea on the total porosity that one can expect to be present in the mosaics. Plotting the equivalent pore diameter (nm) versus the cumulative porosity for sample 4 assuming that the BET porosity does not start at 0% at pore diameters of 100 nm but has a starting porosity calculated with the PSD model ($D = 2.1 \pm 0.06$, $\log C^* = -1.9 \pm 0.35$) results in Fig. 7c, where the size distribution of the PIPS-SEM-data only represents pore areas in the matrix (Houben et al., 2013). For this particular sample the size distribution seems to be best represented by the upper bound of the average power law constant ($D = 2.16$) because of the fact that this is a matrix rich sample. Extrapolated SEM porosity is in the range of 1.7–4% for pores with equivalent diameters down to 2 nm, where the model does fit the adsorption N₂ data better than the Ar data. This extrapolated SEM porosity falls within the He porosity range for similar samples (2–7%; Fig. 7b).

4.2. Comparison of Whitby Mudstone to other shales

4.2.1. Porosity Whitby Mudstone vs. porosity Posidonia Shale

For the Posidonia shale the total porosity has been determined in a number of different ways. Mann (1987) published porosity values between 5 and 20% (specific surface areas of 0.5–18 m²/g) for samples with different maturities using Nitrogen adsorption. Based on a combination of TEM, SEM, and X-ray microtomography the total porosity is between 2 and 5 vol. % according to (Kanitpanyacharoen et al., 2012). Visible SEM porosity for PSF is 2.62–2.74% (Klaver et al., 2012), where the total porosity was estimated to be between 3.9 and 13.8% when assuming the pores not visible in the BIB-SEM mosaics follow a similar pore size distribution ($D \approx 1.9$ – 2.2) as visible pores. Furthermore, the He porosity is 3–16.6% for PSF samples (Ghanizadeh et al., 2014). Although the WMF samples (He porosity = 2–7%) fall in the lower half of the PSF range they do overall show similar porosity values and pores are distributed following a similar size distribution ($2.0 < D < 2.3$ for WMF). In addition, BIB-SEM (Klaver et al., 2012) and μ -CT (Kanitpanyacharoen et al., 2012) results for PSF show that at the resolution used for imaging (down to ca. 10 nm pixel size) pores are not forming connected pore networks, which is in agreement with the WMF BET data showing that more than 90% of the porosity has pore diameters smaller than 10 nm. This implies that pore throats have to be < 10 nm, which is in agreement with what is found for other claystones (Opalinus Clay, Boom clay, Haynesville shale and Bossier shale) using Wood's Metal Injection experiments (Klaver et al., 2015b). The results show that significant volumes of larger pores are not connected via pore throats down to 10 nm in diameter (Klaver et al., 2015b). BET measurements and He porosimetry data show that there are smaller pores present in the samples. This implies that at least the amount of measured Ar/N₂/He porosity is due to pores connected to the samples outside

forming a pore network that is accessible for the different gasses (Ar, N₂, He) used. These pores measured with gas adsorption ($>99\%$ of the pores measured with Ar, N₂ adsorption/desorption), below SEM resolution, should be situated in the matrix due to the fact that this is the only connected medium present in the samples, implying also that any gas flow out of the sample has to find its way through this matrix.

4.2.2. Comparison to other (producing) gas shales

Microstructurally the WMF is a typical shale with silt-sized grains interbedded in a matrix, similar to: Barnett shale (Sondergeld et al., 2010), Eagle Ford shale (Sondergeld et al., 2010), Marcellus shale (Curtis et al., 2012), Posidonia shale (Klaver et al., 2012), Haynesville shale (Curtis et al., 2012; Klaver et al., 2015a), and Bossier shale (Klaver et al., 2015a). The proportion of organic matter pores vs. matrix pores vs. other pores is in the WMF similar to for instance the Bossier shale (Loucks et al., 2012; Klaver et al., 2015a), some of the Haynesville shale samples (Klaver et al., 2015a), and Pearsall shale (Loucks et al., 2012). The Barnett and Fayetteville shales on the other hand show a higher contribution of organic matter pores (Loucks et al., 2012; Bai et al., 2013), suggesting more storage space for gas in the organic matter of these samples but not necessarily also suggesting better connected pathways from the pore network into the fracture network. Comparing SEM porosity values as reported in the literature to values found in this study shows that overall the SEM porosity for gas shales is below 3% (Fig. 8a; e.g.: Klaver et al., 2015a; Klaver et al., 2012; Curtis et al., 2012), whereas the He pycnometer porosity shows a larger range of porosity values, 3–12% (Curtis et al., 2012). These results show that the WMF samples display SEM porosities in the same range as other (gas) shales, whereas they fit to the lower half of the He porosity range possibly implying less connectivity via pore throats of the visible large pores (bodies) present in the SEM images and hence displaying a less favourable pore network for gas extraction than other (gas) shales. In addition, BET surface areas (N₂) show a similar range of values for different gas shales as has been measured in this study (Fig. 8b; Clarkson et al., 2013). The Barnett, Duvernay, Haynesville and Muskwa1 samples show a slightly higher BET surface area (N₂) than measured for the WMF, whereas the Eagleford, Marcellus, Mont2, Muskwa2 and both Woodford samples show values in the same range as the WMF (Clarkson et al., 2013). Furthermore, PSF values for BET surface area are in the same range as found for the WMF and other gas shales (0.5–18 m²/g; Mann, 1987). WMF layered samples show a slightly higher average BET surface area (N₂) than the clay samples implying a slightly higher gas storage capacity or porosity for the layered samples. The higher porosity in the layered samples is mainly due to more and larger pores in the matrix in between the clasts, where it seems that the larger amount of $>2 \mu\text{m}$ grains and the lower amount of matrix caused less compaction of the matrix overall in these samples. This suggests that the lower half of the WMF is more favourable for gas extraction than the upper half of the WMF and in the case of N₂ adsorption does give comparable results to other (gas) shales. This shows that although the pore network that is reachable for He in the WMF is on the low half when compared to other (gas) shales, when N₂ is used for adsorption the reached amount of pores is comparable to that of other (gas) shales showing a similar connected pore network to N₂ gas molecules as that found in other (gas) shales. Plotting the clay content (XRD, XRF) in the samples versus the He porosity shows that there is no clear trend visible (Fig. 8c; Ghanizadeh et al., 2014; Clarkson et al., 2013; Chalmers et al., 2012; Gasparik et al., 2014; Sone and Zoback, 2013) between the porosity and clay content, the same goes for porosity and quartz content and porosity and carbonate content. Comparing our results on mineralogy to that of

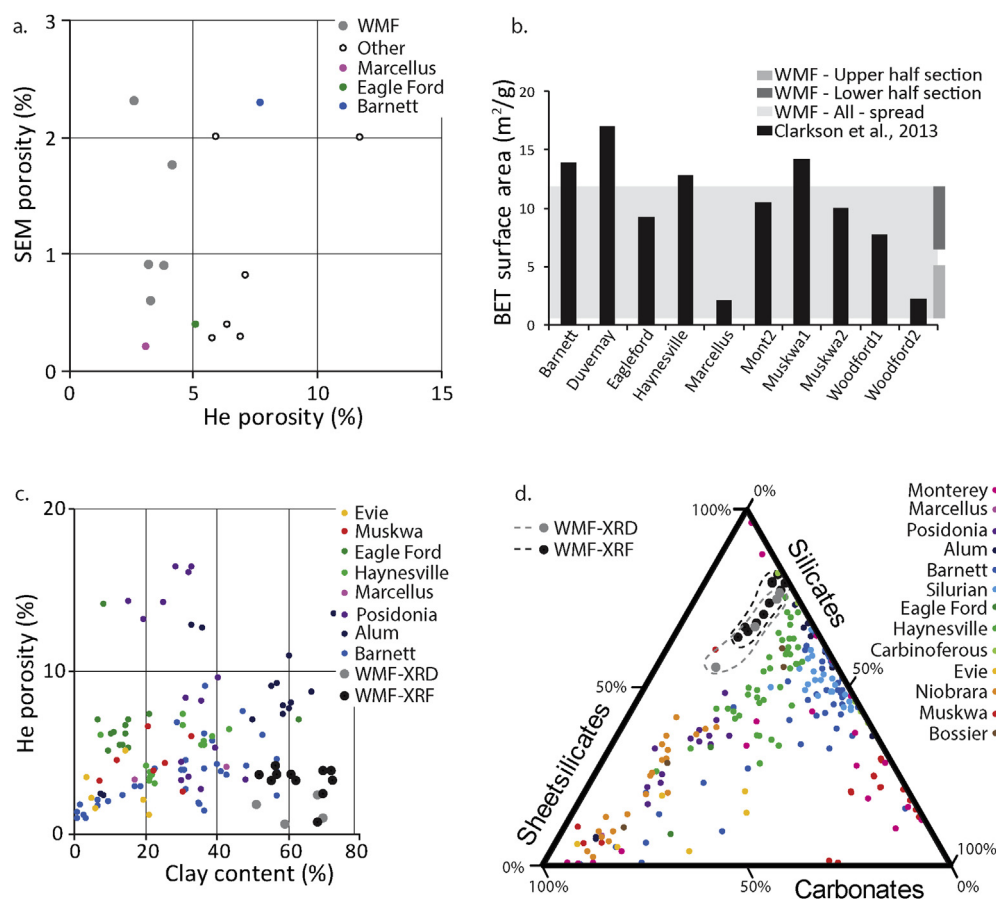


Fig. 8. a. SEM porosity vs. He porosity illustrates that SEM porosity underestimate the total porosity visible in the samples. b. The range of WMF BET surface areas measured falls within the same range as that found in literature for other (producing) gas shales. c. When plotting He porosity vs. clay content it becomes visible that the clay content generally does not influence He porosity, no trend is visible in the shale data. d. WMF mineralogy compared to mineralogy values for (producing) gas shales as found in literature shows that the WMF samples plot on the high sheet silicates end and that mineralogically samples are similar to the Haynesville and Carboniferous shales.

the Posidonia shale (PSF) (XRD: Klaver et al., 2012; Ghanizadeh et al., 2014; Gasparik et al., 2014) shows that the PSF samples have an overall higher carbonate content and lower sheet silicate and silicate contents (Fig. 8d), but comparable quartz content. Microstructurally the PSF samples of the Hils section (Germany; Klaver et al., 2012) are comparable to the upper half of the WMF section, with fossils, quartz, calcite, organic matter, pyrite and mica embedded in a matrix. Mineralogy data is an important factor in gas production from the tight shale systems that require stimulation (Curtis, 2002), where the brittleness of the rock can be related to the mineralogy. Varying clay, quartz and calcite contents for instance result in variable fracture gradients in the Barnett shale (Curtis, 2002; Ross and Bustin, 2009). The WMF mineralogy data (XRD and XRF) can be easily compared to the mineralogy found for other gas shales or gas shale prospects like the Barnett, Haynesville and Eagle Ford shales (Fig. 8d; e.g.: Klaver et al., 2015a; Clarkson et al., 2013; Chalmers et al., 2012; Gasparik et al., 2014; Sone and Zoback, 2013; Ross and Bustin, 2009; Ghanizadeh et al., 2013a; Saidian et al., 2015). Mineralogy of gas shales and gas shale prospects show a big scatter with regard to the amounts of sheet silicates, silicates and carbonates present in the different shales, not only between different formations but also within a formation there is a spread. WMF mineralogy plots in the sheet silicates rich domain and is close in composition to the Haynesville and Carboniferous shales, which could imply that WMF behaves mechanically similar to these two shales. The Monterey shale results are scattered throughout the graph. Barnett, Muskwa, Alum and

Silurian shales are mainly more quartz rich, whereas Evie, Niobrara, Marcellus, Bossier, Posidonia and Eagle Ford shales are more carbonate rich. The Brittleness Index (BI) is a relative measure of the compressive strength of a rock over the tensile strength (e.g.: Yagiz, 2009; Perez Altamar and Marfurt, 2015; Hajiabdolmajid and Kaiser, 2003). Alternatively, Curtis (2002) and Wang and Gale (2009) suggest BI definitions based on mineralogical composition of the rock, where you divide the 'brittle' minerals (e.g.: quartz, dolomite) over the sum of brittle and ductile minerals (e.g.: carbonates, sheet silicates). Both BI definitions (Curtis, 2002; Wang and Gale, 2009) give similar results and can be used to subdivide a stratigraphic section in mineralogically more brittle and more ductile parts (e.g.: for Barnett shale in Perez Altamar and Marfurt, 2015), where the clay minerals are all treated equally and the role of different clay minerals is not clear at the moment. For the WMF samples with silicate contents of 13–18% the BI's based on mineralogy are below 0.2, indicating a ductile to less ductile regime (Perez Altamar and Marfurt, 2015) throughout the WMF. A BI from 0.32 and up would indicate a less brittle to brittle regime. This mineralogy BI should be combined with elastic parameters to give a more robust value resulting in a single brittleness value that can be compared throughout the section and for different shales. In summary, WMF samples plot on the high end for clay content, low end for quartz and carbonate content, displays similar SEM porosities, similar pore characteristics, similar BET N₂ surface areas, and are on the low end for He porosity when compared to other gas shales (Fig. 8a, b, c, d). This could imply that WMF shales are overall less favourable to

mechanically fracture than other (producing) gas shales, and since the porosity is on the low end gas transportation through the matrix might be more difficult and slower in the WMF than found in other (gas) shales.

4.2.3. Permeability WMF inferred from the microstructural investigations

One can get an idea of the matrix permeability of the here investigated samples based on the measured porosity values by for instance using (Yang and Aplin, 1998, 2007; Costa, 2006; Xu and Yu, 2009; Esemie et al., 2012): 1. The Kozeny–Carman equation as described by Yagiz (2009), (Eq. (1)):

$$k = \frac{ds^2}{36S} \frac{\varphi^3}{(1-\varphi)^2} [\text{m}^2] \quad (1)$$

where ds is the average grain size [m] of the samples, S is the Kozeny–Carman constant, and φ is the porosity (Costa, 2006); 2. The Kozeny–Carman equation as described by Leonards (1962) and Yang and Aplin (2007), (Eq. (2)):

$$k = \frac{1}{k_0 k_T} \frac{\varphi^3}{(1-\varphi^2)S^2} [\text{m}^2] \quad (2)$$

where k_0 and k_T are shape and tortuosity factors, S is the specific surface area and φ is the porosity; 3. The Yang–Aplin model (Yang and Aplin, 1998), (Eqs. (3) and (4)):

$$k_v = 10^{-19.21} J_v^{1.118} \bar{r}^{1.074} [\text{m}^2] \quad (3)$$

$$k_h = 10^{-19.21} J_h^{1.118} \bar{r}^{1.074} [\text{m}^2] \quad (4)$$

where k_v is the vertical permeability and k_h is the horizontal permeability, (Eqs. (5)–(7)),

$$J_v = \frac{9}{8} \varphi (\sin(\alpha))^2 \frac{J_1^3}{(1 + J_1 + J_1^2)^2} \quad (5)$$

$$J_h = \frac{9}{8} \varphi (\cos(\alpha))^2 \frac{J_1^3}{(1 + J_1 + J_1^2)^2} \quad (6)$$

$$J_1 = 2.371 - 1.626 \text{clay}^2 + 153.8 \varphi^4 \quad (7)$$

clay is the fractional clay content, r is the mean pore throat radius, φ is the porosity, and α is the average pore alignment angle relative to the bedding. Using these porosity, permeability relations one has to keep in mind that all of the equations use certain assumptions with respect to the pore geometry and pore network geometry, which might not represent the real pore (network) geometry as visible in the SEM images. Assuming permeability of the WMF depends on the grain size of the matrix gives a first hint of the matrix permeability that one can expect in the WMF. Using Eq. (1) assuming the matrix grain size is between 100 nm and 2 μm , taking a Kozeny–Carman constant of 5 (Costa, 2006), and a porosity between 1 and 7% (see He, N_2 and Ar adsorption) the matrix permeability of the WMF can be estimated to be in the range of $5.7 \cdot 10^{-23}$ – $8.8 \cdot 10^{-18} \text{ m}^2$. For Eq. (2) the estimated permeability would be in the $1.2 \cdot 10^{-24}$ – $6.6 \cdot 10^{-19} \text{ m}^2$ range, using; $k_0 k_T$ is 200–1000 (Yang and Aplin, 2007), S is between 1,616,466 and 29,459,976 [m^{-1}] and the porosity is between 1 and 7%. When the Yang–Aplin model (Yang and Aplin, 1998, Eqs. (3)–(7)) is used the

horizontal permeability ranges from $2.3 \cdot 10^{-22}$ to $2.1 \cdot 10^{-21} \text{ m}^2$ and the vertical permeability from $5.7 \cdot 10^{-23}$ – $1.8 \cdot 10^{-22} \text{ m}^2$, using; a clay content between 50 and 75%, a porosity between 1 and 7%, a mean pore throat radius of 5 nm, and an α value between 28° and 18° based on the formulas in Yang and Aplin (1998). Based on the SEM images though the α value is on average between 3° and 5° , changes the permeability range from $4 \cdot 10^{-25}$ – $1 \cdot 10^{-23} \text{ m}^2$ vertically and $3 \cdot 10^{-22}$ – $2 \cdot 10^{-21} \text{ m}^2$ horizontally. Predicted permeability for WMF samples spans thus over six orders of magnitude depending on the input parameters and the formula used (10^{-18} – 10^{-25} m^2). Comparing this to literature values for oil shales (Xu and Yu, 2009) shows that Kozeny–Carman permeability calculated for Messel, Torbanite, Condor, Himmetoglu, and Posidonia shale shows values in the $6.8 \cdot 10^{-24}$ to $5.3 \cdot 10^{-21} \text{ m}^2$ range. Furthermore, pressure step decay measurements (e.g.: Sutherland and Cove, 1980; Peach and Spiers, 1996) on Barnett shale (Vermilyen, 2011), Evie shale (Ross and Bustin, 2009), Muskwa shale (Chalmers et al., 2012), Oil shales (Clarkson et al., 2013), Alum shale (Ghanizadeh et al., 2013b) and Posidonia shale (Ghanizadeh et al., 2014) show methane permeability's measured in the range of $6 \cdot 10^{-20}$ – $2 \cdot 10^{-16} \text{ m}^2$, where the pulse decay measurements seem to result in slightly higher permeability values than the ones predicted using the Kozeny–Carman or Young–Aplin models. This can be explained by the fact that the permeability of rock depends on the sample size (Cui et al., 2009), where the larger the sample the more heterogeneities can influence the permeability. Faults and fractures on the larger scale, but also mineralogical differences and different grains sizes down to the mm scale can influence the any flow through the rocks. Samples for the Pulse Decay method are generally cm scale (diameter 2.5 cm), whereas the permeability values using the mathematical relations are based on the particle size of particles in the matrix ($< 2 \mu\text{m}$). Cui et al. (2009) show that a sample size difference of two orders of magnitude can change the permeability over five orders of magnitude for shales. Furthermore, experiments show that the permeability of mudstones range over ten orders of magnitude (Dewhurst et al., 1999), where the range of permeability at a single porosity decreases with decreasing porosity down to two orders of magnitude for a porosity of 0.15 (Yang and Aplin, 2010). Hence the here calculated values should be checked with permeability experiments on WMF samples.

5. Conclusions

Whitby Mudstone Formation (WMF) is a fine-grained mudstone with silt-sized minerals embedded in a fine-grained matrix, which is microstructurally comparable to the PSF. The WMF section can be subdivided in a carbonate (fossil) rich upper and a carbonate poor sub mm scale mineralogically layered lower half. Overall porosity is in the order of 0.3–6.9% and depends on the method used (for both drying and porosity determination) and the sample investigated. Pores are mainly situated in the matrix (all samples), carbonate fossils (upper half of the section) and some of the organic matter (lower half of the section). An indication of the matrix permeability is calculated using a number of mathematical models and is for the measured porosities in the range of $4.5 \cdot 10^{-24}$ – $8.8 \cdot 10^{-18} \text{ m}^2$. Comparing these values to literature data of the PSF shows similar porosity, permeability and pore size distribution values, illustrating that the WMF could be used as an analogue for the PSF. Mineralogically the WMF plots on the high sheet silicates end of the ternary plot when compared to PSF and other (producing) gas shales and porosity of the WMF would plot in the lower half of the range. This could imply that WMF shales could be less favourable to mechanically fracture than other producing gas shales, and since the porosity is on the low end gas transportation through the matrix might be more difficult.

Acknowledgements

We would like to thank: M. Trogisch (University of Münster; thin section preparation), T. van de Gon Netscher (modification SEM stubs), P. van Krieken (sample preparation), T. de Kruijff (TU Delft, TNW-HREM/NS; PIPS milling), A. den Otter (BET measurements), W. Verwaal (pycnometry and X-ray tomography) and K.-H. Wolf (assistance with XRF data interpretation). TNO is thanked for fruitful collaboration in Whitby (UK) during the WMF sampling campaign. Funding by the Topsector Energy Innovation Program upstream gas (TKIG01017) and our industry partners; EBN, GDF Suez, Wintershall, Total and Baker Hughes is greatly appreciated. In addition, we would like to thank F. Kets and two anonymous reviewers for their helpful reviews.

References

- Bai, B., Elmagati, M., Zhang, H., Wei, M., 2013. Rock characterization of Fayetteville shale gas plays. *Fuel* 105, 645–652.
- Barret, E.P., Joyner, L.G., Halenda, P.P., 1951. The determination of pore volume and area distributions in porous substances. I. computations from nitrogen isotherms. *J. Am. Chem. Soc.* 73, 373–380.
- Bray, R.J., Green, P.F., Duddy, I.R., 1992. Thermal history Reconstruction Using Apatite Fission Track Analysis and Vitrinite Reflectance: a Case Study from the UK East Midlands and Southern North Sea, 67. Geological Society, London, Special Publications, pp. 3–25.
- Bruker, 1999. TOPAS Software. Bruker AXS GmbH, Karlsruhe, Germany.
- Brunauer, S., Emmett, P.H., Teller, E., 1938. Adsorption of gases in multimolecular layers. *J. Am. Chem. Soc.* 60, 309–319.
- Chalmers, G.R.L., Ross, D.J.K., Bustin, R.M., 2012. Geological controls on matrix permeability of Devonian gas Shales in the Horn river and Liard basins, northeastern British Columbia, Canada. *Int. J. Coal Geol.* 103, 120–131.
- Clarkson, C.R., Solano, N., Bustin, R.M., Bustin, A.M.M., Chalmers, G.R.L., He, L., Melnichenko, Y.B., Radlinski, A.P., Blach, T.P., 2013. Pore structure characterization of North American shale gas reservoirs using USANS/SANS, gas adsorption, and mercury intrusion. *Fuel* 103, 606–616.
- Costa, A., 2006. Permeability-porosity relationship: a re-examination of the Kozeny–Carman equation based on a fractal pore-space geometry assumption. *Geophys. Res. Lett.* 33 <http://dx.doi.org/10.1029/2005GL025134>. L02318.
- Cui, X., Bustin, A.M.M., Bustin, R.M., 2009. Measurements of gas permeability and diffusivity of tight reservoir rocks: different approaches and their applications. *Geofluids* 9, 208–223.
- Curtis, M.E., Sondergeld, C.H., Ambrose, R.J., Rai, C.S., 2012. Microstructural investigation of gas shales in two and three dimensions using nanometer-scale resolution imaging. *AAPG Bull.* 96 (4), 665–677.
- Curtis, J.B., 2002. Fractured shale-gas systems. *AAPG Bull.* 86 (11), 1921–1938.
- Desbois, G., Urai, J.L., Kukla, P.A., 2009. Morphology of the pore space in claystones – evidence from BIB/FIB ion beam sectioning and cryo-SEM observations. *E-Earth* 4, 15–22.
- Dewhurst, D.N., Yang, Y., Aplin, A.C., 1999. Permeability and fluid flow in natural mudstones. In: Aplin, A.C., Fleet, A.J., Macquaker, J.H.S. (Eds.), *Muds and Mudstones: Physical and Fluid Flow Properties*, 158. Special publications, Geological Society, London, pp. 23–43.
- Eseme, E., Krooss, B.M., Littke, R., 2012. Evolution of petrophysical properties of oil shales during high-temperature compaction tests: Implications for petroleum expulsion. *Mar. Pet. Geol.* 31, 110–124.
- ESRI, 2012. ArcMap 10.1. In: Arcinfo Desktop 10.1. ESRI, Redlands, California, U.S.
- Gale, J.F., Reed, R.M., Holder, J., 2007. Natural fractures in the Barnett Shale and their importance for hydraulic fracture treatments. *AAPG Bull.* 91 (4), 603–622.
- Gasparik, M., Bertier, P., Gensterblum, Y., Ghanizadeh, A., Krooss, B.M., Littke, R., 2014. Geological controls on the methane storage capacity in organic-rich shales. *Int. J. Coal Geol.* 123, 34–51.
- Ghadeer, S.G., Macquaker, J.H.S., 2011. Sediment transport processes in an ancient mud-dominated succession: a comparison of processes operating in marine offshore settings and anoxic basinal environments. *J. Geol. Soc.* 168, 1121–1132.
- Ghadeer, S.G., Macquaker, J.H.S., 2012. The role of event beds in the preservation of organic carbon in fine-grained sediments: analyses of the sedimentological processes operating during deposition of the Whitby Mudstone formation (Toarcian, Lower Jurassic) preserved in northeast England. *Mar. Pet. Geol.* 35, 309–320.
- Ghanizadeh, A., Gasparik, M., Amann-Hildenbrand, A., Gensterblum, Y., Krooss, B.M., 2013a. Lithological controls on matrix permeability of organic-rich shales: an experimental study. *Energy Procedia* 40, 127–136.
- Ghanizadeh, A., Gasparik, M., Amann-Hildenbrand, A., Gensterblum, Y., Krooss, B.M., 2013b. Experimental study of fluid transport processes in the matrix system of the European organic-rich shales: I Scandinavian Alum Shale. *Mar. Pet. Geol.* 51, 79–99.
- Ghanizadeh, A., Gasparik, M., Amann-Hildenbrand, A., Gensterblum, Y., Krooss, B.M., Littke, R., 2014. Experimental study of fluid transport processes in the matrix system of the European organic-rich shales: II Posidonia Shale. *Int. J. Coal Geol.* 123, 20–33.
- Green, P.F., 1989. Thermal and tectonic history of the East Midlands shelf (onshore UK) and surrounding regions assessed by apatite fission track analysis. *J. Geol. Soc.* 146, 755–773.
- Groen, J.C., Peffer, L.A.A., Pérez-Ramírez, J., 2003. Pore size determination in modified micro- and mesoporous materials. Pitfalls and limitations in gas adsorption data analysis. *Microporous mesoporous Mater.* 60, 1–17.
- Hajiabdoalmajid, V., Kaiser, P., 2003. Brittleness of rock and stability assessment in hard rock tunnelling. *Tunn. Undergr. Space Technol.* 18, 35–48.
- Harkins, W.D., Jura, G., 1944. A vapour adsorption method for the determination of the area of a solid without the assumption of a molecular area, and the areas occupied by nitrogen and other molecules on the surface of a solid. *Surfaces solids XIII*, 1366–1373.
- Heath, J.E., Dewers, T.A., McPherson, B.J.O.L., Petrusak, R., Chidsey Jr., T.C., Rinehart, A.J., Mozley, P.S., 2011. Pore networks in continental and marine mudstones: characteristics and controls on sealing behavior. *Geosphere* 7 (2), 429–454. <http://dx.doi.org/10.1130/GES00619.1>.
- Hemmingway, J.E., Riddler, G.P., 1982. Basin inversion in north Yorkshire. *Trans. Inst. Min. Metall. Sect. B* 91, 175–186.
- Herber, R., de Jager, J., 2010. Oil and gas in the Netherlands – is there a future? *Neth. J. Geosci.* 89–2, 91–107.
- Hesselbo, S.P., Gröcke, D.R., Jenkyns, H.C., Bjerrum, C.J., Farrimond, P., Morgans Bell, H.S., Green, O.R., 2000. Massive dissociation of gas hydrate during a Jurassic oceanic anoxic event. *Lett. Nat.* 406, 392–395.
- Higgins, M.D., 2000. Measurement of crystal size distribution. *Am. Mineral.* 85, 1105–1116.
- Houben, M.E., Desbois, G., Urai, J.L., 2013. Pore morphology and distribution in the shaly facies of Opalinus Clay (Mont Terri, Switzerland): insights from representative 2D BIB-SEM investigations on mm to nm scale. *Appl. Clay Sci.* 71, 82–97.
- Houben, M.E., Desbois, G., Urai, J.L., 2014. A comparative study of representative 2D microstructures in Shale and Sandy facies of Opalinus Clay (Mont Terri, Switzerland) inferred from BIB-SEM and MIP methods. *Mar. Pet. Geol.* 49, 143–161.
- Houben, M.E., 2013. In Situ Characterisation of the Microstructure and Porosity of Opalinus Clay (Mont Terri Rock Laboratory, Switzerland). Fakultät für Georesourcen und Materialtechnik RWTH Aachen University, p. 192. Dissertation.
- Imber, J., Armstrong, H., Clancy, S., Daniels, S., Herringshaw, L., McCaffrey, K., Rodrigues, J., Trabucho-Alexandre, J., Warren, C., 2014. Natural fractures in a United Kingdom shale reservoir analog, Cleveland Basin, northeast England. *AAPG Bull.* 98 (11), 2411–2437.
- Jackson, M.L., Sayin, M., Clayton, R.N., 1976. Hexafluorosilicic acid reagent modification for quartz isolation. *soil Sci. soc. Am. J.* 40, 958–960.
- Jarvie, D.M., Hill, R.J., Ruble, T.E., Pollastro, R.M., 2007. Unconventional shale-gas systems: the Mississippian Barnett Shale of north-central Texas as one model for thermogenic shale-gas assessment. *AAPG Bull.* 91 (4), 475–499.
- Jenkyns, H.C., Clayton, C.J., 1997. Lower Jurassic epicontinental carbonates and mudstones from England and Wales: chemostratigraphic signals and the early Toarcian anoxic event. *Sedimentology* 44, 687–706.
- Jenkyns, H.C., 1985. The early Toarcian and Cenomanian-Turonian anoxic events in Europe: comparisons and contrasts. *Geol. Rundsch.* 74 (3), 505–518.
- Kameda, A., Dvorkin, J., Keehm, Y., Nur, A., Bosl, W., 2006. Permeability-porosity transforms from small sandstone fragments. *Geophysics* 71 (1), N11–N19.
- Kanitpanyacharoen, W., Kets, F.B., Wenk, H.-R., Wirth, R., 2012. Mineral preferred orientation and microstructure in the Posidonia shale in relation to different degrees of thermal maturity. *Clays Clay minerals* 60, 315–329.
- Keller, L.M., Holzer, L., Wepf, R., Gasser, P., 2011. 3D geometry and topology of pore pathways in Opalinus clay: Implications for mass transport. *Appl. Clay Sci.* 52, 85–95.
- Kemp, D.B., Coe, A.L., Cohen, A.S., Schwark, L., 2005. Astronomical pacing of methane release in the early Jurassic period. *Nature* 437, 396–399.
- Ketcham, R.A., Hanna, R.D., 2014. Beam hardening correction for X-ray computed tomography of heterogeneous natural materials. *J. Comput. Geosci.* 67, 49–61.
- Klaver, J., Desbois, G., Urai, J.L., Littke, R., 2012. BIB-SEM study of the pore space morphology in early mature Posidonia Shale from the Hils area, Germany. *Int. J. Coal Geol.* 103, 12–25.
- Klaver, J., Desbois, G., Urai, J.L., Littke, R., 2015a. BIB-SEM characterization of pore space morphology and distribution in post mature to over mature samples from the Haynesville and Bossier shales. *Mar. Pet. Geol.* 59, 451–466.
- Klaver, J., Hemes, S., Houben, M., Desbois, G., Radi, Z., Urai, J.L., 2015b. The connectivity of pore space in mudstones: insights from high-pressure Wood's metal injection, BIB-SEM imaging, and mercury intrusion porosimetry. *Geofluids* 15 (4). <http://dx.doi.org/10.1111/gfl.12128>.
- Knox, R.W.O.'B., Howard, A.S., Powell, J.H., Buchem, van, F.S.P., 1991. Lower and middle Jurassic sediments of the Cleveland Basin, N.E. England: shallow marine and paralic facies seen in their sequence stratigraphical context. In: 13th International Sedimentological Congress, Field Guide No. 5, 1990. British Sedimentological Research Group, Cambridge, p. 66.
- Leythaeuser, D., Littke, R., Radke, M., Schaefer, R.G., 1988. Geochemical effects of petroleum migration and expulsion from Toarcian source rocks in the Hils syncline area, NW-Germany. *Adv. Org. Geochem.* 13, 489–502.
- Leonards, G.H., 1962. *Engineering Properties of Soils*. McGraw-Hill, New York.
- Littke, R., Baker, D.R., Leythaeuser, D., Rullkötter, J., 1991. Keys to the depositional history of the Posidonia Shale (Toarcian) in the Hils Syncline, northern Germany. from. In: Tyson, R.V., Pearson, T.H. (Eds.), *Modern and Ancient*

- Continental Shelf Anoxia, 58. Geological Society Special Publication, p. 331.
- Loucks, R.G., Reed, R.M., Ruppel, S.C., Hammes, U., 2012. Spectrum of pore types and networks in mudrocks and a descriptive classification for matrix-related mudrock pores. *AAPG Bull.* 96 (6), 1071–1098.
- Mann, U., 1987. Veränderung von Mineralmatrix und Porosität eines Erdölmuttergesteins durch einen Intrusivkörper (Lias epsilon 2-3: Hilsmulde, NW-Deutschland). *Facies* 17 (1), 181–188.
- Moore, D.M., Reynolds, R.C., 1997. X-ray Diffraction and the Identification and Analysis of Clay Minerals, second ed. Oxford university press.
- Nakashima, S., Hasegawa, D., Kishida, K., Yasuhara, H., 2010. Measurement of fracture Aperture in granite core using Microfocus X-ray CT. In: Paper ARMA 10-205 Presented at the 44th US Rock Mechanics Symposium and 5th U.S.–Canada Rock Mechanics Symposium, Held in Salt Lake City, UT, USA, June 27–30 2010.
- Olphen van, H., 1977. An Introduction to Clay Colloid Chemistry: for Clay Technologists, Geologists and Soil Scientists, second ed. Wiley, New York, p. 315.
- Passey, Q.R., Bohacs, K.M., Esch, W.L., Klimentidis, R., Sinha, S., 2010. From Oil-prone Source Rock to Gas-producing Shale Reservoir – Geologic and Petrophysical Characterization of Unconventional Shale-gas Reservoirs. *SPE* 131350, <http://dx.doi.org/10.2118/131350-MS>.
- Peach, C.J., Spiers, C.J., 1996. Influence of crystal plastic deformation on dilatancy and permeability development in synthetic salt rock. *Tectonophysics* 256, 101–128.
- Perez Altamar, R., Marfurt, K., 2015. Mineralogy-based brittleness prediction from surface seismic data: application to the Barnett Shale. *Interpretation* 2 (4), T255–T271.
- Powell, J.H., 2010. Jurassic sedimentation in the Cleveland Basin: a review. *Proc. Yorks. Geol. Soc.* 58 (1), 21–72.
- Raiswell, R., 1976. The microbiological formation of carbonate concretions in the upper Lias of NE England. *Chem. Geol.* 18, 227–244.
- Raiswell, R., 1982. Pyrite texture, isotopic composition, and the availability of iron. *Am. J. Sci.* 282, 1244–1263.
- Regelink, J.A., 2014. Mincomp – A Program to Calculate a Likely Mineralogical Bulk Composition from XRD and XRF Results. Research Minor Report. Delft University of Technology, 81pp. <http://repository.tudelft.nl/view/ir/uuid:b026ed6a-aba0-450b-9f28-3066a057bdb0/>.
- Rietveld, H.M., 1967. Line profiles of neutron powder-diffraction peaks for structure refinement. *Acta Cryst.* 22, 151.
- Ross, D.J.K., Bustin, R.M., 2009. The importance of shale composition and pore structure upon gas storage potential of shale gas reservoirs. *Mar. Pet. Geol.* 26, 916–927.
- Rullkötter, J., Leythaeuser, D., Horsfield, B., Littke, R., Mann, U., Müller, P.J., Radke, M., Schaefer, R.G., Schenk, H.-J., Schwochau, K., Witte, E.G., Welte, D.H., 1988. Organic matter maturation under the influence of a deep intrusive source: a natural experiment for quantitation of hydrocarbon generation and expulsion from a petroleum source rock. *Adv. Org. Geochem.* 13, 847–856.
- Saelen, G., Telnaes, N., Raiswell, R., 1995. Environmental conditions during deposition of organic-rich sediments in the Whitby Mudstone formation (Toarcian), England. In: Grimalt, J.O., Dorronsoro, C. (Eds.), *Organic Geochemistry: Developments and Applications to Energy, Climate, Environment and Human History*, 17th International Meeting on Organic Geochemistry, A.I.G.O.A., Donostia, San Sebastian, pp. 224–226.
- Saelen, G., Doyle, P., Talbot, M.R., 1996. Stable-isotope analyses of belemnite rostra from the Whitby Mudstone Formation, England: surface water conditions during deposition of a marine black shale. *Palaios* 11, 97–117.
- Saidian, M., Kuila, U., Rivera, S., Godinez, L.J., Prasad, M., 2015. Porosity and Pore Size Distribution in Mudrocks: A Comparative Study for Haynesville, Niobrara, Monterey and Eastern European Silurian Formation. In: *Unconventional Resources Technology Conference*, Denver, Colorado, USA, 25–27 August 2014. <http://dx.doi.org/10.15530/urtec-2014-1922745>.
- Scarlett, N.V.Y., Madsen, I.C., 2006. Quantification of phases with partial or no known crystal structure. *Powder Diff.* 21 (4), 278–284.
- Sondergeld, C.H., Ambrose, R.J., Rai, C.S., Moncrieff, J., 2010. Micro-structural studies of gas shales, SPE. In: *Unconventional Gas Conference*, Pittsburgh, Pennsylvania, USA, 23–25 February 2010.
- Sone, H., Zoback, M.D., 2013. Mechanical properties of shale-gas reservoir rocks – Part 1: Static and dynamic elastic properties and anisotropy. *Geophysics* 78 (5), D381–D392.
- Šrodoň, J., Drits, V.A., McCarty, D.K., Hsieh, J.C.C., Eberl, D.D., 2001. Quantitative X-ray diffraction analysis of clay-bearing rocks from random preparations. *Clays Clay minerals* 49 (6), 514–528.
- Sutherland, H.J., Cove, S.P., 1980. Argon gas permeability of New Mexico rock salt under hydrostatic compression. *Int. J. Rock Mech. Min. Sci. Geomech. Abstr.* 17, 281–288.
- The Math Works, 2011. MATLAB 2011. The MathWorks, Natick, MA, USA.
- Trabucho-Alexandre, J., Dirks, R., Veld, H., Klaver, G., Boer, de, P.L., 2012. Toarcian black shales in the Dutch central graben: record of energetic, variable depositional conditions during an oceanic anoxic event. *J. Sediment. Res.* 82, 104–120.
- Vermeylen, J.P., 2011. PhD-thesis. Geomechanical studies of the Barnett Shale, Texas, USA, 25. Stanford University, p. 143.
- Wang, F.P., Gale, J.F.W., 2009. Screening criteria for shale-gas systems. *Gulf Coast Assoc. Geol. Soc. Trans.* 59, 779–793.
- Wignall, P.B., Newton, R., 1998. Pyrite framboid diameter as a measure of oxygen deficiency in ancient mudrocks. *Am. J. Sci.* 298, 537–553.
- Wignall, P.B., Newton, R.J., Little, C.T.S., 2005. The timing of paleoenvironmental change and cause-and-effect relationships during the early Jurassic mass extinction in Europe. *Am. J. Sci.* 305, 1014–1032.
- Williams, P.F.V., 1986. Petroleum geochemistry of the Kimmeridge Clay of onshore southern and eastern England. *Mar. Pet. Geol.* 3 (4), 258–281.
- Wolf, K.-H.A.A., 2006. The interaction between underground coal fires and their roof rocks. Dissertation. TU Delft, the Netherlands, 90-9020939-5. 978-90-9020939-5.
- Xu, P., Yu, B., 2009. Developing a new form of permeability and Kozeny-Carman constant for homogeneous porous media by means of fractal geometry. *Adv. water Resour.* 31, 74–81.
- Yagiz, S., 2009. Assessment of brittleness using rock strength and density with punch penetration test. *Tunn. Undergr. Space Technol.* 24, 66–74.
- Yang, Y., Aplin, A.C., 1998. Influence of lithology and compaction on the pore size distribution and modelled permeability of some mudstones from the Norwegian margin. *Mar. Pet. Geol.* 15, 163–175.
- Yang, Y., Aplin, A.C., 2007. Permeability and petrophysical properties of 30 natural mudstones. *J. Geophys. Res.* 112 <http://dx.doi.org/10.1029/2005JB004243>. B03206.
- Yang, Y., Aplin, A.C., 2010. A permeability-porosity relationship for mudstones. *Mar. Pet. Geol.* 27, 1692–1697.
- Zhubayev, A., Houben, M.E., Smeulders, D.M.J., Barnhoorn, A., 2015, 2016. Ultrasonic velocity and attenuation anisotropy of shales, Whitby, United Kingdom. *Geophysics* 81 (1), D45–D56. <http://dx.doi.org/10.1190/GEO2015-0211.1>.
- Ziegler, P.A., 1982. Geological Atlas of Western and Central Europe, Shell International Petroleum. Elsevier, Maatschappij.